Early Evolution of Himalayan Orogenic Belt and Generation of Middle Eocene Magmatism: Constraint From Haweng Granodiorite Porphyry in the Tethyan Himalaya

Wei-Qiang Ji[1]*, Fu-Yuan Wu[1], Jia-Min Wang[1], Xiao-Chi Liu[1], Zhi-Chao Liu[2], Zhiyong Zhang[1], Wenrong Cao[3], Jian-Gang Wang[1] and Chang Zhang[1]

[1] State Key Laboratory of Lithospheric Evolution, Institute of Geology and Geophysics, Chinese Academy of Sciences, Beijing, China, [2] School of Earth Sciences and Engineering, Sun Yat-sen University, Guangzhou, China, [3] Department of Geological Sciences and Engineering, University of Nevada, Reno, Reno, NV, United States

Although the Himalayan orogenic belt is dominant by Oligocene to Miocene leucogranites, it initiated magmatic activity from middle Eocene. However, the exact distribution and genesis of early magmatism are yet to be resolved. This study identified new outcrops of middle Eocene magmatism, Haweng granodiorite porphyries, from northwest Langkazi in the northern Tethyan Himalaya, southern Tibet. Identical zircon U–Pb ages were obtained by secondary ion mass spectrometry (17JT13: 45.3 ± 0.4 Ma; 17JT16: 44.5 ± 0.8 Ma) and laser ablation inductively coupled plasma mass spectrometry (LA-ICP-MS) (17JT15: 44.3 ± 0.8 Ma; 12FW75: 44.4 ± 0.6 Ma) methods for different outcrops there. Titanite LA-ICP-MS U–Pb analyses also gave consistent lower intercept ages for samples 17JT13 (45.3 ± 0.5 Ma) and 17JT15 (44.5 ± 0.6 Ma). Zircon metamorphic rims of sample 17JT15 recorded a younger thermal event of 29.9 ± 0.4 Ma. The analyzed samples possess high SiO_2 (69.98–73.53 wt.%), Al_2O_3 (15.07–16.15 wt.%), variable Na_2O (3.94–5.81 wt.%) with Na_2O/K_2O ratios of 1.57–7.88, and A/CNK values of 1.08–1.27 indicative of sodic peraluminous series. They show variable Sr (342–481 ppm) and Rb (37.9–133 ppm) concentrations and low Rb/Sr ratios (0.10–0.39), radiogenic Sr isotopes [$^{87}Sr/^{86}Sr_{(t)}$: 0.7190–0.7251], and unradiogenic Nd–Hf isotopes with $\varepsilon_{Nd}(t)$ values of −13.54 to −11.55 and $\varepsilon_{Hf}(t)$ values of −11.97 to −9.37, respectively. The variation of major and trace elements, such as increases in Na_2O and Sr and decreases in K_2O and Rb, resulted from cumulation of plagioclase and crystal fractionation of K-feldspar during magma evolution. The Haweng granodiorite porphyries were derived from partial melting of dominant amphibolites and variable metasedimentary rocks. The newly identified outcrops help conform the EW trending middle Eocene magmatic belt along the Yarlung Tsangpo suture zone, resulting from breakoff of the Neo-Tethyan slab at *ca.* 45 Ma.

Keywords: middle Eocene magmatism, granodiorite porphyry, Tethyan Himalaya, high Sr/Y, slab breakoff

INTRODUCTION

The Cenozoic Himalayan orogeny was accompanied by long-lasting magmatism. Deciphering the petrogenesis of these magmatic rocks is therefore a key issue to understand the formation and evolution of the orogenic belt. The Himalaya initiated crustal anatexis from middle Eocene after the India–Asia continental collision (Zeng et al., 2011; Hou et al., 2012; Carosi et al., 2015; and references therein), which lasted until late Miocene (*ca.* 44–7 Ma, Wu et al., 2015, 2020). Melt generation and granite emplacement are mainly related to the exhumation stage of the Greater Himalayan Sequence (GHS) during the late Oligocene to early Miocene (Harris and Massey, 1994; Hodges, 2000; Searle, 2013; Zeng and Gao, 2017).

With respect to this dominant magmatic stage, less attention has been paid to the magmatism during prograde metamorphism, especially initial stage of partial melting. The early partial melting includes two main styles: (1) anatexis during prograde/peak metamorphism of the GHS as reflected by anatectic melt inclusions within garnet (Carosi et al., 2015, 2019; Iaccarino et al., 2015) and (2) partial melting of thickened lower crust along the northern margin of Himalaya (Aikman et al., 2008; Zeng et al., 2011; Hou et al., 2012). Although evidence of early anatexis during prograde metamorphism was reported from frontal Himalaya, the ubiquitous existences of monazites of this stage preclude the possibility of widely partial melting, as the melting would consume monazites and erase their records of earlier metamorphism (Gibson et al., 2004; Kohn et al., 2005). The early magmatism, which is of relatively large scale and has been dated by zircon U–Pb method, is locally distributed and limited to the Yardoi dome and adjacent area from northeastern Himalaya (Aikman et al., 2008; Zeng et al., 2011; Hou et al., 2012). Furthermore, only some coeval granitic dikes were found in the Ramba dome (Liu et al., 2014).

Thus, more outcrops of Himalayan granites are necessary to reveal the distribution and generation of early Cenozoic magmatism, which is important to constrain the deep dynamic process of Himalayan orogenic evolution. And this study identified new exposure of middle Eocene granitic rocks from northwest of Langkazi county along the north margin of Himalaya. Zircon U–Pb age and Hf isotope, whole-rock element and Sr–Nd–Hf isotopes are invoked to reveal the petrogenesis and early evolution of the Himalayan orogenic belt.

GEOLOGICAL BACKGROUND AND SAMPLES

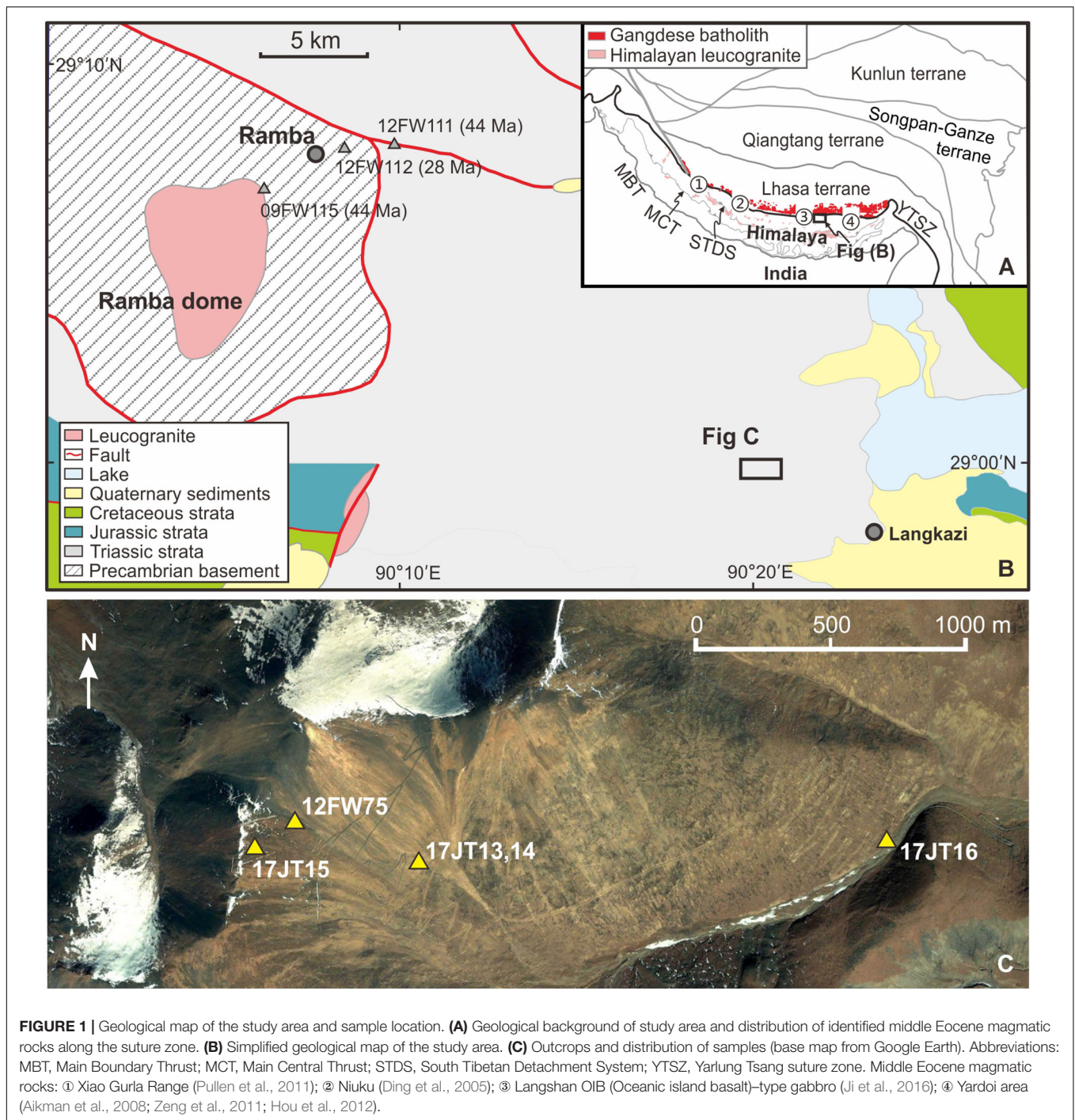## Geological Units of Southern Tibet

The Himalayan–Tibetan orogenic belt was generated by the India–Asia continental collision, which initiated at around 60 Ma along the Yarlung Tsangpo suture zone (YTSZ) (Wu et al., 2014; Hu et al., 2016; and references therein). It consists of several east–west trending geological blocks, namely, the Himalaya, Lhasa, Qiangtang, Songpan–Ganze, and Kunlun terranes from south to north. To the south of YTSZ, the Lhasa terrane was an active continental margin (the Gangdese arc) accompanying the

northward Neo-Tethyan subduction (Searle et al., 1987). The arc magmatic activity in the southern margin of the Lhasa terrane lasted from middle Triassic to Eocene (cf. Wen et al., 2008; Ji et al., 2009; Wang et al., 2016) until the breakoff of the Neo-Tethyan oceanic slab at around 45 Ma (Ji et al., 2016 and references therein).

The Himalaya, to the south of YTSZ, can be divided into four tectonic belts including the Sub-Himalaya, the Lesser Himalayan Sequence (LHS), the GHS, and the Tethyan Himalayan Sequence (THS), separated by several faults and shear zones including the Main Boundary Thrust (MBT), the Main Central Thrust (MCT), and the South Tibetan Detachment System (STDS) (**Figure 1A**) (Hodges, 2000; Yin, 2006). The Sub-Himalaya, the southernmost and structurally lowest lithotectonic belt, is composed of the synorogenic sedimentary units of the Siwalik Group, bounded at the top by the MBT. In the hanging wall of the MBT, the LHS encompasses Paleoproterozoic to early Mesoproterozoic metasedimentary rocks, and Paleoproterozoic granites. Bound by the MCT at the base and STDS at the top, the GHS is the metamorphic core of the Himalaya comprising high-grade metasedimentary and meta-igneous rocks with age ranging from Neoproterozoic to Ordovician. The GHS was intruded by leucogranitic rocks of various scales varying from sills and dikes to plutons, especially in its upper part blew the brittle strand of the STDS (Debon et al., 1986; Searle et al., 2010). Above the STDS, the THS consists of continuous sedimentary sequence from Paleozoic to Eocene, which belongs to a passive continental margin during the northward Neo-Tethyan subduction. The THS has been deformed during the Cenozoic India–Asia collision, but the metamorphic grade is very low with the highest of greenschist facies.

Early Cenozoic Evolution of Southern Tibet

After the initial India–Asia continental collision, the Indian continent began to underthrust beneath the southern margin of Asia continent (i.e., the Lhasa terrane) because of drag of the attached Neo-Tethyan oceanic slab. The shallow crust of Indian continent was decoupled and stayed at the top, forming the THS, whereas the deep crust was dragged to various depths, parts of which exhumed later in the form of (ultra) high-pressure rocks, such as the eclogites in the Kagan Valley and Tso Morori in the northwest Himalaya (e.g., de Sigoyer et al., 2000; Kaneko et al., 2003), and the GHS extruded southward between the MCT and the STDS (Burchfiel et al., 1992; Le Fort, 1996). The YTSZ and adjacent regions underwent fast crustal thickening after initial collision as indicated by crustal deformation, development of fold and thrust belt, and magmatism. These N-S contractional structures were intruded by undeformed middle Eocene granitic rocks (45–44 Ma) in several locations along the YTSZ (Ding et al., 2005; Pullen et al., 2011). As the leading edge of collision belt, regions adjacent to the YTSZ were prone to obtain thickened crust first, and they already had thickened crust by middle Eocene suggested by the widespread development of adakitic rocks along strike (e.g., Guan et al., 2012; Ji et al., 2012; Liu et al., 2014; Ma et al., 2014; Shellnutt et al., 2014). They should have maintained

FIGURE 1 | Geological map of the study area and sample location. **(A)** Geological background of study area and distribution of identified middle Eocene magmatic rocks along the suture zone. **(B)** Simplified geological map of the study area. **(C)** Outcrops and distribution of samples (base map from Google Earth). Abbreviations: MBT, Main Boundary Thrust; MCT, Main Central Thrust; STDS, South Tibetan Detachment System; YTSZ, Yarlung Tsang suture zone. Middle Eocene magmatic rocks: ① Xiao Gurla Range (Pullen et al., 2011); ② Niuku (Ding et al., 2005); ③ Langshan OIB (Oceanic island basalt)–type gabbro (Ji et al., 2016); ④ Yardoi area (Aikman et al., 2008; Zeng et al., 2011; Hou et al., 2012).

the thickest crust of the Tibet with a present thickness greater than 70 km on the basis of geophysical observation (cf. Zhao et al., 2001; Nábělek et al., 2009).

The early process of crustal thickening was not limited to the suture zone but propagated southward quickly. The THS, the structurally highest units of the Himalayan orogenic belt, developed horizontal shortening and regional fold and thrust belt during early–middle Eocene (*ca.* 50–45 Ma: Ratschbacher et al., 1994; Wiesmayr and Grasemann, 2002), and the main stage of

shortening and crustal thickening for the shallow crust could have completed prior to middle Eocene (44.1 ± 1.2 Ma, Aikman et al., 2008 and references therein). The crustal thickening was documented by early Eocene growth of garnet in the middle crust in the Mabja (54–52 Ma) and Kangmar (51–49 Ma) domes from central Himalaya (Smit et al., 2014). In the eastern Himalaya, the schists from Yardoi dome underwent Eocene (48–36 Ma) prograde metamorphism (Ding et al., 2016a,b). The authors regarded these upper crust rocks as part of the upper

level of the GHS, which were buried to 20–30 km due to shallow subduction of the Indian continent beneath the Lhasa terrane. The garnet amphibolite and granitic gneiss recorded high amphibolite and granulite facies metamorphism in the Yardoi dome at 45.0 ± 1.0 and 47.6 ± 1.8 Ma, respectively, followed by anatexis at 43.5 ± 1.3 Ma (Zeng et al., 2011; Gao et al., 2012). The middle Eocene granitic rocks (46–42 Ma) from Yardoi dome and adjacent areas show adakitic affinities indicating thickened crust already occurred at that time (Zeng et al., 2011; Hou et al., 2012). Thus, southern Tibet was located in an N-S compressional setting in the early Cenozoic, accompanied with continental subduction, structural shortening, crustal thickening, and prograde metamorphism.

The study area is located in the north margin of the THS (**Figure 1A**). Grandiorite porphyry outcrops were identified from the Haweng deposit, northwest of the Langkazi County (**Figure 1B**). The granodiorite porphyry intruded into the late Triassic Nieru Formation, consisting of slate, siltstone, meta-sandstone, and crystalline limestone, as dikes or stocks of different scale from the mountainside to the mountain ridge/peak (**Figures 1C**, **2**). Samples 17JT13 and 17JT14 were collected from the same outcrop in the mountainside (**Figure 1C**). The granodiorite porphyry here intruded into the sandstone of Nieru Formation and developed sandstone enclave (**Figure 2**). Sample 12FW75 was collected in a higher location close to the mountain ridge, whereas sample 17JT15 was from the mountain ridge, namely, a small peak. The outcrop of sample 17JT15 was of large scale with severely cracked intrusive rocks at the top (**Figure 2A**). Sample 17JT16 was a rolling stone collected in the valley, which has least mafic minerals and is different from the investigated outcrop samples. It is used to reveal the potential magmatic evolution. All the intrusive rocks show porphyritic texture (**Figures 2C,D**), and the phenocrysts are mainly plagioclase, quartz, K-feldspar, small biotite, and a some muscovite (**Figures 2E,F**), whereas the accessory minerals include zircon, apatite, and titanite.

ANALYTICAL METHODS

Zircon secondary ion mass spectrometry (SIMS) U–Pb dating for samples 17JT13 and 17JT16 and laser ablation inductively coupled plasma mass spectrometry (LA-ICP-MS) U–Pb and Hf isotopic analysis for sample 12FW75 were performed at the Institute of Geology and Geophysics, Chinese Academy of Sciences (IGGCAS), Beijing, China. Cathodoluminescence (CL) images were used for selection of zircon grain and dating position. Zircon SIMS U–Pb dating was conducted using a Cameca IMS-1280, following the analytical procedures described by Li et al. (2009). The ellipsoidal spot is approximately 10×15 μm in size. Calibration of Pb/U ratios is relative to the standard zircon Plešovice. Zircon LA-ICP-MS U–Pb analysis for sample 12FW75 was performed on an Agilent 7500a Q-ICP-MS equipped with a 193-nm Excimer ArF laser ablation system (Geolas plus), using zircon 91500 as external standard with circle spot of 30 μm in diameter. The detailed analytical procedures for zircon U–Pb age can be found in Xie

et al. (2008). Zircon Hf isotopic analyses were conducted on the dated spots by the MC-ICPMS method (Wu et al., 2006) using a Thermo-Finnigan Neptune multicollector connected to the same laser ablation system. Data reduction was carried out using Isoplot/Ex v 3.0 program (Ludwig, 2003). The in-house zircon U–Pb age standard for SIMS analysis, Qinghu, yielded $^{206}Pb/^{238}U$ age of 160.8 ± 1.7 Ma [Mean Square of Weighted Deviates (MSWD), = 0.34, $n = 8$], whereas the zircon standards for LA-ICP-MS analyses gave a mean age of 604.6 ± 6.4 Ma (MSWD = 0.13, $n = 13$) for GJ1. These obtained standard ages are consistent with the recommended values (Elhlou et al., 2006; Li et al., 2009). The $^{176}Hf/^{177}Hf$ ratios for zircons GJ1 and Mud Tank are 0.282010 ± 9 (MSWD = 4.2, $n = 24$) and 0.282506 ± 6 (MSWD = 3.1, $n = 21$), respectively, agreeing well with the recommended values (Woodhead and Hergt, 2005; Elhlou et al., 2006).

Zircon (17JT15) and titanite (17JT13 and 17JT15) U–Pb analyses were performed at the Beijing Quick-Thermo Science & Technology Co., Ltd., using an ESI New Wave NWR 193^{UC} (TwoVol2) laser ablation system connected to an Agilent 8900 ICP–QQQ. Individual zircon/titanite grains (mounted and polished in epoxy) were ablated in a constant stream of He that is mixed downstream with N_2 and Ar before entering the torch region of the ICP–QQQ. After warm-up of the ICP–QQQ and connection with the laser ablation system, the ICPMS is first tuned for robust plasma conditions by optimizing laser and ICP–QQQ setting and monitoring $^{232}Th^{16}O^+/^{232}Th^+$ ratios (always ≤ 0.2%) and $^{238}U^+/^{232}Th^+$ ratios (always between 0.95 and 1.05), while ablating NIST SRM 612 in line scan mode. 91500 zircon and Plešovice zircon were used as primary and secondary reference materials, respectively, for zircon U–Pb age determination. OLT-1 titanite and Fish Canyon Tuff titanite were used as primary and secondary reference materials, respectively, during titanite U–Pb age determination. Background subtraction and correction for laser downhole elemental fractionation were performed using the Iolite data reduction package within the Wavemetrics Igor Pro data analysis software (Paton et al., 2010). The analytical spots for zircon and titanite are 15 and 40 μm in diameter, respectively. Plešovice zircon gave mean ages of 337.7 ± 2.4 Ma (MSWD = 0.1, $n = 31$), whereas the titanite standard (Fish Canyon Tuff) had a lower intercept of 29.2 ± 1.0 Ma (MSWD = 2.6; $n = 44$). These dating results for LA-ICP-MS analyses are consistent with the recommended values within errors (Schmitz and Bowring, 2001; Sláma et al., 2008).

Whole-rock major and trace elements were measured by PANalytical Axios XRF and Agilent 7700x ICP-MS, respectively, at ALS Chemex Company (Guangzhou, China). The analytical precision and accuracy for major elements are better than 5 and 2%, respectively, and for trace elements are better than 10 and 10%, respectively. Whole-rock Sr–Nd–Hf isotopes of Sample 12FW75 were separated in a combined procedure from a single sample digestion according to the procedure of Yang et al. (2010), and then $^{87}Sr/^{86}Sr$, $^{143}Nd/^{144}Nd$, and $^{176}Hf/^{177}Hf$ were analyzed by multicollector inductively coupled plasma mass spectrometry (MC-ICP-MS) at IGGCAS following the methods of Yang et al. (2010, 2011a,b), respectively. The total procedural blanks measured for Lu, Hf, Rb, Sr, Sm, and Nd were less than 10, 50,
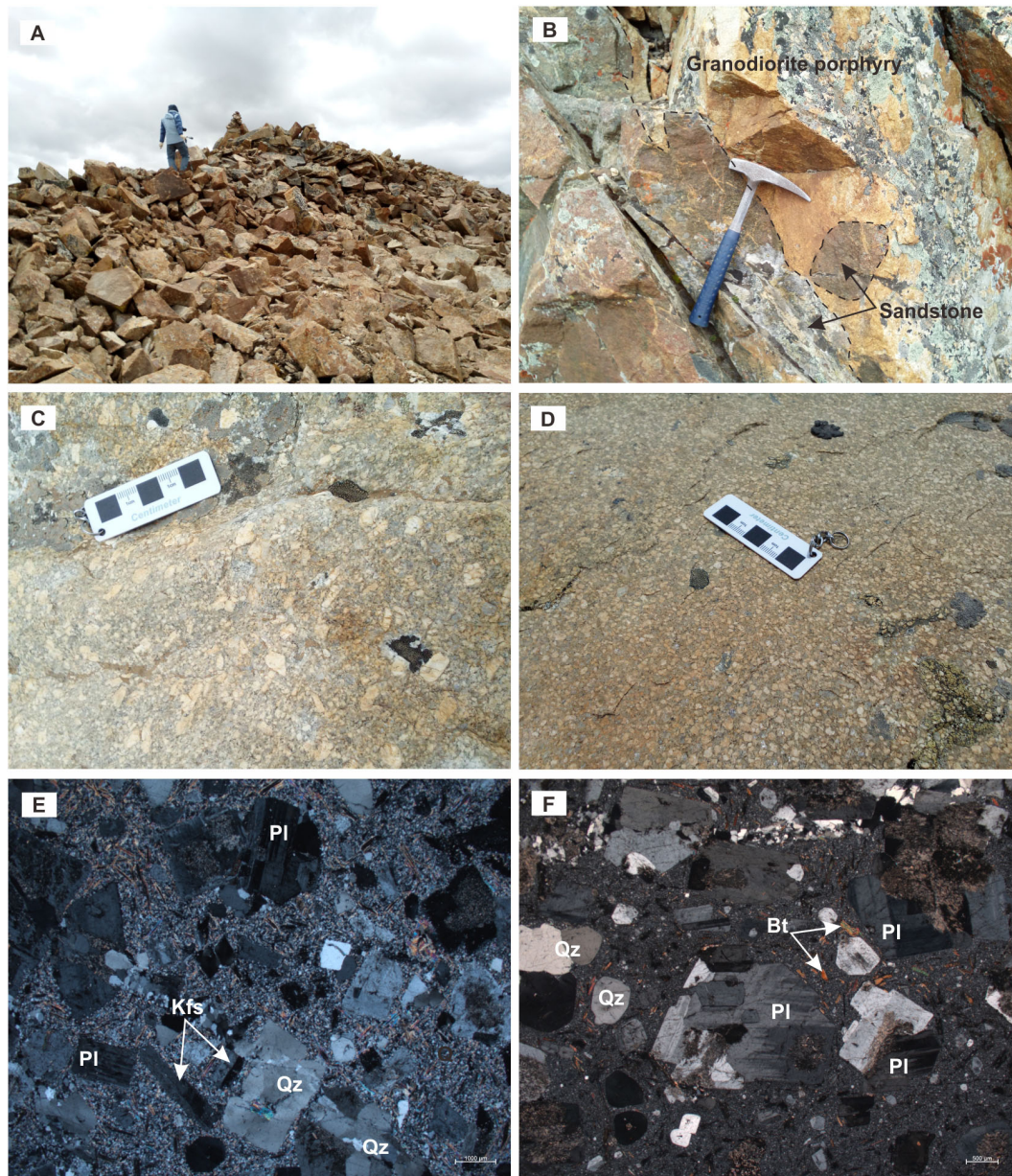
FIGURE 2 | Field pictures and micrographs for Haweng granodiorite porphyries. **(A,C,E)** Are for sample 17JT15, whereas **(B,D,F)** are for sample 17JT13. Abbreviations: Bt, biotite; Kfs, K-feldspar; Pl, plagioclase; Qz, quartz.

50, 100, 50, and 50 pg, respectively. The $^{87}Sr/^{86}Sr$, $^{143}Nd/^{144}Nd$, and $^{176}Hf/^{177}Hf$ ratios were normalized to $^{87}Sr/^{86}Sr = 0.1194$, $^{143}Nd/^{144}Nd = 0.7219$, and $^{176}Hf/^{177}Hf = 0.7325$ by exponential law, respectively. During the period of data acquisition, standards yielded results of $^{87}Sr/^{86}Sr = 0.710248 \pm 0.000007$ (2 SD, $n = 6$) for NBS987, $^{143}Nd/^{144}Nd = 0.512108 \pm 5$ (2 SD, $n = 6$) for Jndi-1, and $^{176}Hf/^{177}Hf = 0.282184 \pm 4$ (2 SD, $n = 7$) for Alfa Hf 14374. In addition, USGS reference materials AGV-2 was also processed for Sr–Nd–Hf isotopes and yielded ratios of 0.703991 ± 11 for $^{87}Sr/^{86}Sr$, 0.512784 ± 14 for $^{143}Nd/^{144}Nd$, and 0.282965 ± 10 for $^{176}Hf/^{177}Hf$, respectively, which are identical

within error, to the recommended values (Weis et al., 2006, 2007). Sr–Nd–Hf isotopic analyses for samples 17JT13–17JT16 were carried out at Nanjing FocuMS Technology Co. Ltd., following a similar method. Geochemical reference materials of USGS BCR-2, BHVO-2, AVG-2, and RGM-2 were treated as quality control. Their isotopic results (BCR-2: $^{87}Sr/^{86}Sr = 0.705001 \pm 4$, $^{143}Nd/^{144}Nd = 512633 \pm 2$, $^{176}Hf/^{177}Hf = 0.282873 \pm 2$; BHVO-2: $^{87}Sr/^{86}Sr = 0.703516 \pm 5$, $^{143}Nd/^{144}Nd = 512976 \pm 2$, $^{176}Hf/^{177}Hf = 0.283087 \pm 2$; RGM-2: $^{87}Sr/^{86}Sr = 0.704373 \pm 3$, $^{143}Nd/^{144}Nd = 512791 \pm 2$, $^{176}Hf/^{177}Hf = 0.283008 \pm 1$; STM-2: $^{87}Sr/^{86}Sr = 0.703700 \pm 4$, $^{143}Nd/^{144}Nd = 512909 \pm 2$,

^{176}Hf/^{177}Hf = 0.283025 ± 2) agree with previous publication within analytical uncertainty (Weis et al., 2006, 2007). The initial Sr–Nd–Hf isotopes in **Table 1** were corrected by t = 45 Ma.

RESULTS

Zircon and Titanite U–Pb Ages and Zircon Hf Isotope

The zircon U–Pb SIMS (17JT13 and 17JT16) and LA-ICP-MS (12FW75 and 17JT15) dating results are listed in **Supplementary Tables 1**, **2**, respectively. Most of the separated zircons have core–rim textures. The cores are irregular, whereas most rims developed oscillatory zonings (**Figure 3A**). We mainly selected dating positions on the rims with enough sizes, but some are in the center for zircons without core–rim textures (**Figure 3B**). Some zircons from sample 17JT15 developed additional narrow rims, which are black in the CL images without oscillatory zoning. This results in core–mantle–rim textures that the mantles developed oscillatory zonings similar to rims of other zircons.

Eighteen zircons from sample 17JT13 were dated by SIMS method, but only 14 of them are available, whereas the others did not give valid data. All the dating spots have high contents of U (1,664–11,349 ppm) and Th (245–1,549 ppm) and relatively low Th/U ratios (0.05–0.18). The dating spots yield ^{206}Pb/^{238}U age of 42.8 to 50.8 Ma. Except for two younger dates (43.0 ± 0.7 and 42.8 ± 0.6 Ma) and two older dates (48.3 ± 0.8 and 50.8 ± 0.8 Ma), the other 10 dating results are clustered (44.1 to 46.1 Ma) and weighted as 45.3 ± 0.4 Ma (n = 10; MSWD = 0.57) (**Figure 4A**). The two younger ones were not consistent with the majority within error and may undergo lead loss. With regard to sample 17JT16, eight dating spots out of 18 ones gave useful dates. They also show high concentrations of U (3,176–12,345 ppm) and Th (150–746 ppm) and relatively low Th/U ratios (0.02–0.17). Except spot 17JT16@09-r (48.4 ± 0.7 Ma), the other seven dates give identical ^{206}Pb/^{238}U age (43.5–46.0 Ma), yielding a weight mean of 44.5 ± 0.8 Ma (n = 7; MSWD = 1.5) (**Figure 4B**) identical to that of sample 17JT13.

Samples 17JT15 and 12FW75 were dated by zircon LA-ICP-MS U–Pb method. Zircons from sample 17JT15 show various textures (**Figure 3B**); for example, uniform, core–rim or core–mantle–rim, and the zircon mantles and rims have enough sizes and were dated by dating spot of 15 μm. Most dating spots yield Eocene ^{206}Pb/^{238}U ages from 43.3 to 45.9 Ma and give a weight mean of 44.3 ± 0.8 Ma (n = 13; MSWD = 0.29) (**Figure 4C**), identical to the other dated samples. Some dates from the narrow dark rims yield Oligocene ^{206}Pb/^{238}U ages of 29.2 to 30.9 Ma weighted at 29.9 ± 0.4 Ma (n = 7; MSWD = 0.59). These younger population displays evidently higher contents of Th (593–5,180 ppm) and U (13,670–36,100 ppm) than the Eocene group (Th = 159–2,920 ppm; U = 1,120–6,030 ppm). The Th/U ratios of the Oligocene dates (0.02–0.14) are much lower than the Eocene ones (0.03–1.04). Sixteen dating results were obtained for sample 12FW75 using analytical spot of 30 μm (**Figure 3D**). The dating spots gave high contents of U (878–10,261 ppm) and Th (132–1,207 ppm) with Th/U ratios from

0.03 to 0.34. The ^{206}Pb/^{238}U ages range from 43.0 to 51.9 Ma. With the exception of three elder spots (49.0, 50.0, and 51.9 Ma), the others yield a weight mean of 44.4 ± 0.6 Ma (n = 12; MSWD = 0.70) (**Figure 4D**), similar to the other dating results within error.

Titanites were separated from two samples (17JT13 and 17JT15) of Haweng granodiorite porphyries and were subjected to LA-ICP-MS U–Pb dating, and the dating results are listed in **Supplementary Table 3**. Except spot 17JT13#25, the other 29 analyses of sample 17JT13 are plotted on the discordia line with a lower intercept of 45.3 ± 0.5 Ma (MSWD = 1.2) (**Figure 4E**). The weighted mean of ^{207}Pb-corrected ^{206}Pb/^{238}U ages for sample 17JT13 shows an identical age of 45.5 ± 0.3 Ma (n = 29; MSWD = 1.10). All the analyses of sample 17JT15 are plotted on the discordia line, intercepting the concordia curve at 44.5 ± 0.6 Ma (MSWD = 1.7, n = 30) (**Figure 4F**). Their ^{207}Pb-corrected ages gave a weighted mean of 44.7 ± 0.4 Ma (MSWD = 1.5; n = 30).

We conducted zircon *in situ* Hf isotopic analysis for sample 12FW75, which are mostly on the dating spots or adjacent realm with consistent CL characteristics with spot size of 40 μm. The analytical results are listed in **Supplementary Table 4**. All the dated zircons show similar Hf isotopic compositions with ^{176}Hf/^{177}Hf of 0.282389 to 0.282545. The corresponding $\varepsilon_{Hf}(t)$ values range from −12.58 to −7.04 with crustal model ages mainly of Paleoproterozoic (1,570–1,921 Ma).

Whole-Rock Geochemistry

Whole-rock major element, trace element, and Sr–Nd–Hf isotope analytical results are listed in **Table 1** and presented in **Figures 5–7**. The analyzed samples show low LOI (loss on ignition) values (1.09–2.60 wt.%), suggesting they are fresh. They exhibit high SiO_2 (69.98–73.53 wt.%), Al_2O_3 (15.07–16.15 wt.%), and Na_2O (3.94–5.81 wt.%); moderate CaO (1.83–2.85 wt.%); and high Na_2O/K_2O ratios (1.57–7.88) (**Figure 5**). They have A/CNK values of 1.08 to 1.27, indicative of peraluminous series (A/CNK > 1). Some samples possess evidently high Na_2O/K_2O ratios due to much lower K_2O contents (0.72–0.79 wt.%).

These samples have rare earth elements (REE) contents of 93–134 ppm, large REE fractionation with La_N/Sm_N = 3.9–4.3 and La_N/Yb_N = 37.7–45.7 (N denotes chondrite normalized value), and weak Eu anomalies [Eu/Eu* = $2Eu_N/(Sm + Gd)_N$] from 0.82 to 0.88. They are relatively enriched in large ion lithophile elements (LILE, e.g., Rb, Ba, Th, and U) and light REEs (LREE, e.g., La and Ce) and relatively depleted in high field strong elements (e.g., Nb, Ta, and Ti) and heavy REEs (HREEs) in the primitive-mantle normalized spidergrams (**Figure 6**). All samples display spikes of Pb in spidergrams and depletions of Ba relative to other LILE. Furthermore, these granodiorite porphyry samples show high Sr concentrations (342–481 ppm), high Sr/Y ratios (63–86 ppm), and low Rb/Sr ratios (0.10–0.39) (**Figures 5G,H**).

The analyzed samples display similar Sr–Nd–Hf isotopic compositions (**Figure 7**). They have low ^{87}Rb/^{86}Sr ratios (0.2898–1.1252), and their measured ^{87}Sr/^{86}Sr ratios range from 0.719206 to 0.725827 with initial ^{87}Sr/^{86}Sr ratios [^{87}Sr/^{86}Sr$_{(t)}$] of 0.7190 to 0.7251. They have unradiogenic Nd and Hf isotopic compositions with ^{143}Nd/^{144}Nd of 0.511920–0.512024 and ^{176}Hf/^{177}Hf of

TABLE 1 | Whole-rock geochemical compositions for Haweng granodiorite porphyries.

Sample	12FW75	17JT13	17JT14	17JT15	17JT16	Sample	12FW75	17JT13	17JT14	17JT15	17JT16
wt.%						Dy	1.18	1.11	1.01	1.13	1.26
SiO_2	69.98	71.37	72.19	73.53	71.48	Ho	0.19	0.19	0.17	0.19	0.22
TiO_2	0.21	0.20	0.20	0.20	0.20	Er	0.44	0.45	0.43	0.45	0.52
Al_2O_3	15.96	15.70	15.35	15.07	16.15	Tm	0.07	0.06	0.06	0.07	0.07
TFe_2O_3	1.32	1.35	1.37	1.33	1.29	Yb	0.38	0.38	0.37	0.44	0.38
MnO	0.02	0.02	0.02	0.02	0.02	Lu	0.06	0.06	0.06	0.06	0.05
MgO	0.78	0.78	0.79	0.79	0.67	Hf	5.46	3.5	3.6	3.8	3.9
CaO	2.14	2.28	2.03	1.83	2.85	Ta	0.88	0.6	0.7	0.8	0.6
Na_2O	3.94	5.81	5.67	4.16	5.30	Pb	122	52.4	48.2	91.7	40.9
K_2O	2.51	0.76	0.72	1.60	0.79	Th	12.77	10.60	10.15	12.20	11.10
P_2O_5	0.09	0.05	0.04	0.08	0.07	U	4.75	4.84	4.21	5.58	4.43
LOI	2.60	1.09	1.55	1.45	1.24	Na_2O/K_2O	1.57	7.64	7.88	2.60	6.71
Total	99.55	99.49	99.99	100.14	100.14	A/CNK	1.22	1.08	1.11	1.27	1.09
ppm						ΣREE	102	94	93	103	107
Li	14.5	13.3	18.7	26.5	17.6	Eu/*Eu	0.82	0.84	0.86	0.88	0.85
Sc	2.7	3.1	2.9	3.0	3.3	Sr/Y	63	77	86	63	82
V	20	15	20	18	12	$(La/Yb)_N$	42	37	38	35	43
Cr	8	8	10	7	2	Rb/Sr	0.39	0.10	0.11	0.29	0.12
Co	1.8	2.8	2.1	2.3	1.6	$^{87}Rb/^{86}Sr$	1.1252	0.2898	0.2964	0.8643	0.3158
Ni	6.6	8.0	7.6	7.4	2.8	$^{87}Sr/^{86}Sr$	0.725827	0.719206	0.720111	0.724641	0.722206
Cu	1.1	1.2	0.6	0.8	0.8	2SE	0.000022	0.000006	0.000006	0.000006	0.000006
Zn	36	35	36	34	34	$^{87}Sr/^{86}Sr(t)$	0.7251	0.7190	0.7199	0.7241	0.7220
Ga	21.0	20.6	21.0	23.0	21.7	$^{147}Sm/^{144}Nd$	0.1225	0.1252	0.1223	0.1205	0.1161
Rb	133	37.9	46.8	100	56.8	$^{143}Nd/^{144}Nd$	0.511992	0.512019	0.512024	0.511986	0.511920
Sr	342	379	412	349	481	2SE	0.000010	0.000004	0.000004	0.000004	0.000004
Y	5.4	4.9	4.8	5.5	5.9	$\varepsilon_{Nd}(0)$	−12.61	−12.07	−11.98	−12.72	−14.00
Zr	128	106	113	116	114	$\varepsilon_{Nd}(t)$	−12.18	−11.66	−11.55	−12.29	−13.54
Nb	6.1	4.1	4.6	5.8	5.2	$f_{Sm/Nd}$	−0.38	−0.36	−0.38	−0.39	−0.41
Cs	12.81	4.29	4.87	6.44	4.84	$T_{DM1}Nd$	1,929	1,941	1,872	1,898	1,914
Ba	460	324	278	417	325	$T_{DM2}Nd$	1,841	1,799	1,790	1,850	1,952
La	23.8	20.9	21.1	23.1	24.2	$^{176}Lu/^{177}Hf$	0.0016	0.0024	0.0024	0.0022	0.0018
Ce	43.9	42.6	42.2	46.7	48.6	$^{176}Hf/^{177}Hf$	0.282407	0.282481	0.282435	0.282467	0.282407
Pr	5.23	4.70	4.66	5.03	5.18	2SE	0.000007	0.000007	0.000007	0.000007	0.000007
Nd	19.4	16.6	16.2	18.2	19.1	$\varepsilon_{Hf}(0)$	−12.90	−10.28	−11.94	−10.77	−12.90
Sm	3.93	3.44	3.28	3.63	3.67	$\varepsilon_{Hf}(t)$	−11.96	−9.37	−11.02	−9.85	−11.97
Eu	0.90	0.81	0.80	0.91	0.92	$T_{DM1}Hf$	1,211	1,133	1,199	1,147	1,220
Gd	2.45	2.22	2.15	2.47	2.70	$T_{DM}{}^CHf$	1,874	1,710	1,814	1,740	1,874
Tb	0.26	0.24	0.23	0.24	0.28	$f_{Lu/Hf}$	−0.95	−0.93	−0.93	−0.93	−0.95

0.282407–0.282481. The corresponding $\varepsilon_{Nd}(t)$ and $\varepsilon_{Hf}(t)$ values are −13.54 to −11.55 and −11.97 to −9.37, respectively. The two-stage Nd-depleted mantle model ages (1,790–1,952 Ma) and the crustal model age of Hf isotope (1,710–1,874 Ma) are similar and both of Paleoproterozoic.

DISCUSSION

Geochronology of Haweng Granodiorite Porphyry and Coeval Himalayan Magmatism

Zircon and titanite have high closure temperatures for the U–Pb system as indicated by previous studies, such as >800°C for zircon (Cherniak and Watson, 2001) and 660–700°C for titanite (Scott and St-Onge, 1995). The Haweng granodiorite porphyries intruded the Triassic sedimentary rocks and were exposed in a shallow level of crust, implying fast cooling and crystallization; thus, both zircon and titanite U–Pb ages can constrain the magma crystallization time. Based on zircon U–Pb dating for samples collected from different outcrops in the Haweng area, four identical $^{206}Pb/^{238}U$ ages were obtained from 44.3 ± 0.8 to 45.3 ± 0.4 Ma. The titanite U–Pb dating results for samples 17JT13 and 17JT15 gave consistent middle Eocene ages (*ca.* 45 Ma). It is interesting that sample 17JT15 shows two age groups, that is, 44.3 ± 0.8 and 29.9 ± 0.4 Ma. As the older zircon population is identical to titanite U–Pb dating results, it should represent the magma crystallization age. The younger age group from the black zircon rims reflects a later event of zircon overgrowth or recrystallization, possibly under low temperature

FIGURE 3 | Representative cathodoluminescence (CL) images for zircons from Haweng granodiorite porphyries. The analytical spots for SIMS method **(A,C)** are elliptic of 10 × 15 μm in size, whereas the LA-ICP-MS spots are circular, 15 μm for 17JT15 **(B)** and 30 μm for 12FW75 **(D)**.
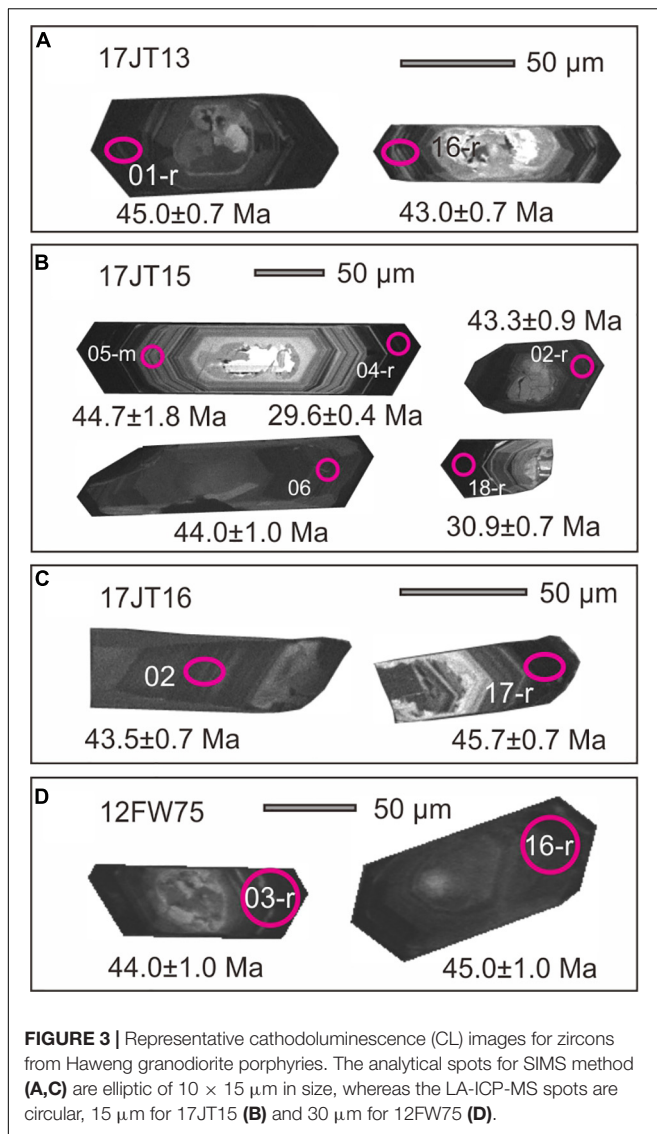
and fluid-assisted condition because the granodiorite porphyries have no obvious metamorphism or deformation. Furthermore, five older spots were obtained from the dated zircon rims from 48.3 to 51.9 Ma including samples 17JT13, 17JT16, and 12FW75. There are two possible explanations for these early Eocene ages. First, they are antecrysts, growing earlier at prograde metamorphic conditions. Second, these analytical results are contaminated by older inherited core, as the dated rims are narrow and thin.

In the east of Ramba dome, Liu et al. (2014) obtained similar U–Pb ages for the porphyritic two-mica granite gneiss (dikes) with 09FW115 of 44.3 ± 0.5 Ma and 12FW111 of 44.1 ± 0.8 Ma (**Figure 1B**). Another sample (12FW112) from different dike with similar lithology there yielded Oligocene U–Pb age (28.2 ± 5.2 Ma, $n = 2$). If the three younger dates (27.8–32.8 Ma) of this sample are included for average calculation, they would give a mean of 29.5 ± 6.2 Ma, which resembles the younger rim age of sample 17JT15 (29.9 ± 0.4 Ma) within error. These similar
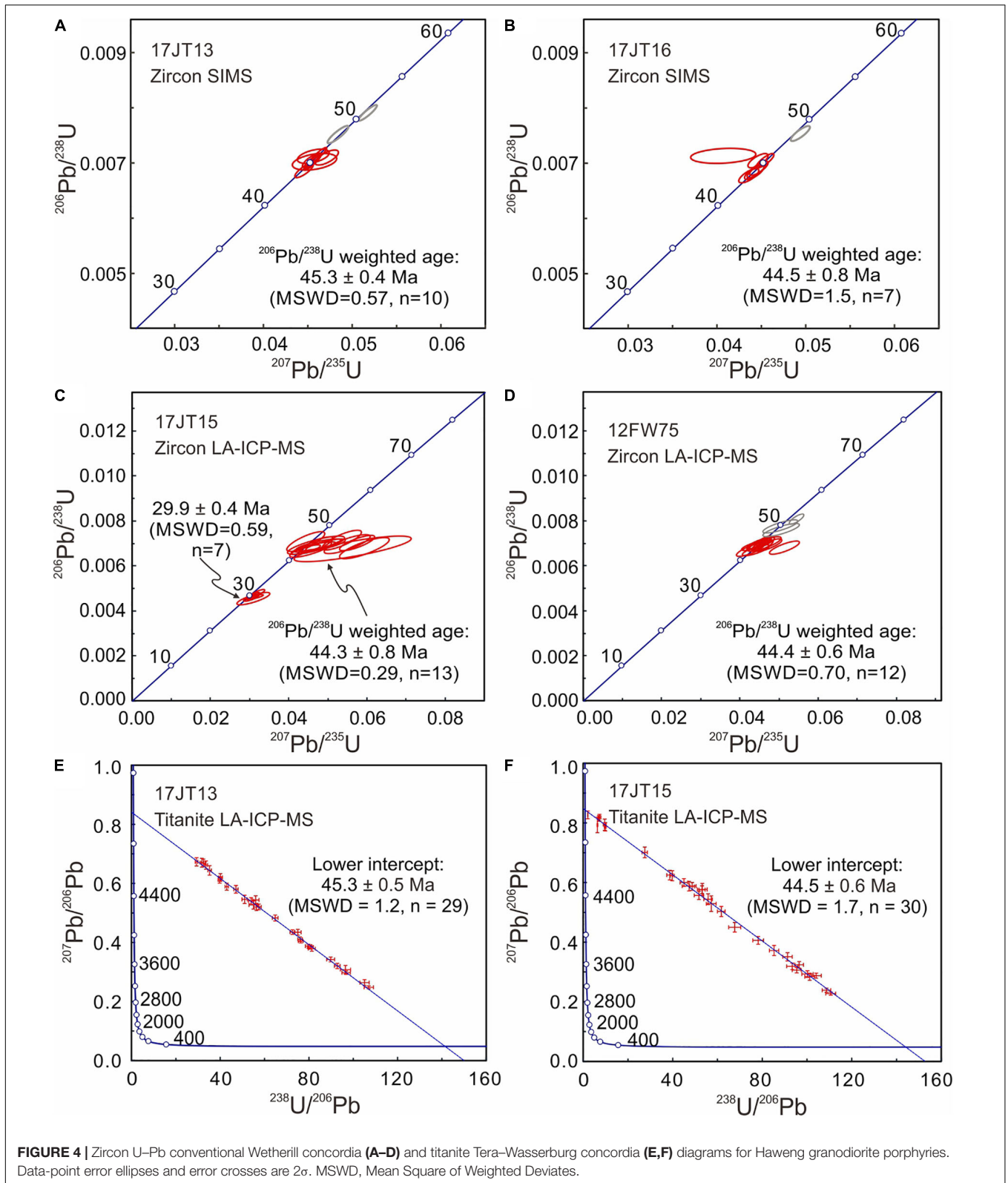
radiometric ages document the existence of early Oligocene thermal event (*ca.* 30 Ma) in the study area, which has been reported along the YTSZ (e.g., Chen et al., 2015).

It is noteworthy that middle Eocene magmatism represents the earliest magmatic activity in the Himalayan orogenic belt after initial continental collision. Previously reported middle Eocene granite plutons are limited to Yardoi dome and adjacent areas, such as Dala and Quedang, in the northeastern Himalaya (number 4 in **Figure 1A**; Aikman et al., 2008; Zeng et al., 2011, 2015; Hou et al., 2012). This study identified new outcrops of middle Eocene magmatism in the Haweng area. Together with the coeval granitic dikes in Ramba dome (Liu et al., 2014), Langkazi–Ramba area is another important region for middle Eocene granitic magmatism, and there may exist intrusion of larger scale but has not been exposed on the basis of field characters. If the suture belt area is taken into account, some small plutons intruded the mélange of YTSZ, such as granite in Xiao Gurla Range (43.9 ± 0.9 Ma, number 1 in **Figure 1A**; Pullen et al., 2011) and Niuku leucogranite (44.8 ± 2.6 Ma, number 2 in **Figure 1A**; Ding et al., 2005). Evidence of this magmatic activity is also documented by abundant middle Eocene inherited zircons in the Miocene dikes intruding northern Tethyan Himalaya and YTSZ in the Xigaze area (Ji et al., 2020). The overall spatial distribution of middle Eocene magmatic activities is located in an east–west trending belt along the northern Himalayan margin.

Magma Nature and Source Characters

Haweng granodiorite porphyries display variable phenocryst contents on outcrops and micrographs, indicative of magma evolution. SiO_2 and Al_2O_3 have a negative correlation, suggesting fractional crystallization of Al-bearing minerals, such as plagioclase, K-feldspar, and biotite. Large variations occur in some major and trace elements, such as Na_2O, Na_2O/K_2O, Rb, and Sr (**Figure 5**). K_2O, Rb, and Ba show close correlations, and they are all compatible in K-feldspar, whereas Na_2O is dominated by plagioclase. Sample 17JT13 with lower K_2O contents (0.76 wt.%) has less K-feldspar phenocrysts, whereas sample 17JT15 has higher K_2O contents (1.60 wt.%) and more K-feldspar phenocrysts (**Figure 2E**). The samples enriched in Sr possess high Na_2O contents (**Figure 5F**), probably indicating cumulation of plagioclase. The three high-Sr samples show negative correlation between Sr and Na_2O may suggest crystal fractionation of K-feldspar, which are also enriched in Sr.

Sample 12FW75 has the lowest SiO_2 and Na_2O and highest K_2O, and it may represent the least evolutional melt of Haweng granodiorite porphyries. As the Haweng granodiorite porphyries and Ramba Eocene porphyritic two-mica granitic dikes (09FW115 and 12FW111) were coeval and spatially adjacent, they may have close generic link and were considered together for study of magma nature. Sample 12FW111 has the lowest SiO_2 (67.62 wt.%) of middle Eocene rocks (**Figure 5**); thus, it may represent primitive component. The Ramba Eocene dikes possess higher Rb and lower Sr contents and weaker depletion of Nb and Ta than other Eocene granitic rocks (**Figure 6**). If the relatively primitive magma was characterized by high Rb and low Sr, the enrichment of Sr was related to cumulation of plagioclase as the samples enriched in Sr have high Na_2O

FIGURE 4 | Zircon U–Pb conventional Wetherill concordia **(A–D)** and titanite Tera–Wasserburg concordia **(E,F)** diagrams for Haweng granodiorite porphyries. Data-point error ellipses and error crosses are 2σ. MSWD, Mean Square of Weighted Deviates.

(**Figure 5F**). The modeling calculation based on Ba and Rb suggests that fractional crystallization of K-feldspar can account for their decreasing trend for Haweng granodiorite porphyries

(**Figure 5H**). This process would lead to evident decrease in Sr and Eu contents, as well as Eu/Eu* values; however, this is not the case for the middle Eocene granites. A potential
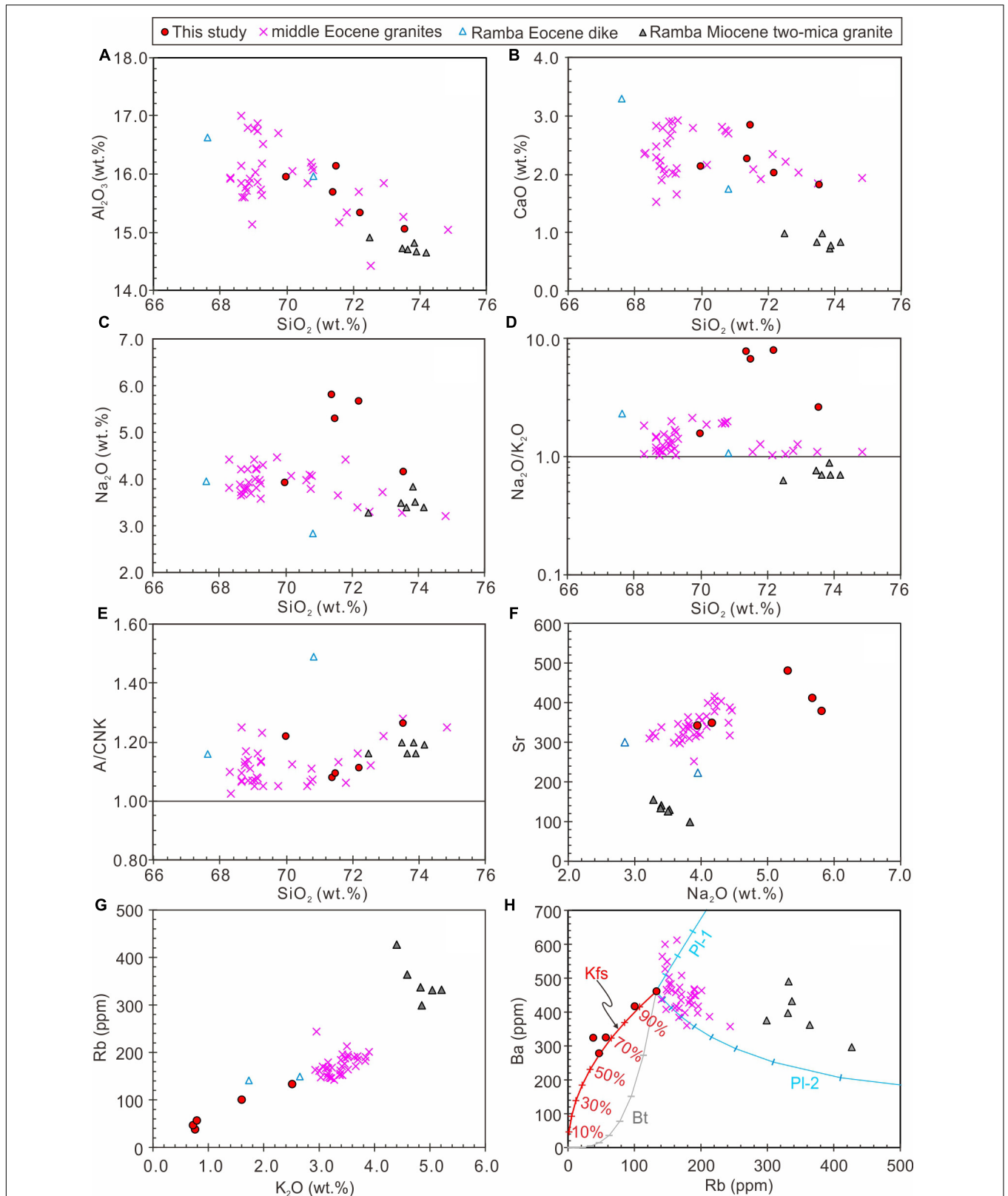
FIGURE 5 | Variation diagrams for selected major and trace elements. Variations of **(A)** Al_2O_3, **(B)** CaO, **(C)** Na_2O, **(D)** Na_2O/K_2O, **(E)** A/CNK vs. SiO_2. Variations of **(F)** Sr vs. Na_2O, **(G)** Rb vs. K_2O, and **(H)** Ba vs. Rb. The numbers in percent of (H) denote melt fractions. The partition coefficients of Rb and Ba for K-feldspar (Kfs) (Rb: 3; Ba: 2), plagioclase (Pl) (Pl-1: Rb = 0.03, Ba = 0.1; Pl-2: Rb = 0.3, Ba = 1.5), and biotite (Bt) (Rb: 2.5; Ba: 6) are from Laurent et al. (2013). Data sources: middle Eocene granites: Zeng et al. (2011) and Hou et al. (2012); Ramba Eocene dike and Miocene two-mica granite: Liu et al. (2014).

FIGURE 6 | Chondrite-normalized REE variation diagram **(A)** and primitive mantle-normalized spider diagrams **(B)** for samples of this study. The normalization data are from Sun and McDonough (1989). Data sources: middle Eocene granitic rocks: Zeng et al. (2011) and Hou et al. (2012); Ramba Eocene dike (12FW111): Liu et al. (2014).

(orange lines in **Figure 7A**). They can also be generated by mixing source (blue lines in **Figure 7A**) between amphibolite and metapelite (end-member F) with the contribution of amphibolites of 50% to 70% (blue lines in **Figure 7A**). In **Figure 7B**, the analyzed samples are all located above the crustal array line (Vervoort et al., 1999), in consistence with potential involvement of mature crustal materials in the magma source. Based on the CL images, most of the zircons developed core–rim textures, and the existence of ancient zircon cores (Liu et al., 2014) suggests important contribution of ancient Himalayan metasedimentary rocks. The Haweng granodiorite porphyries were plotted between middle Eocene granites and Himalayan leucogranites in the Sr–Nd–Hf diagrams (**Figure 7**); thus, they have more involvement of metasedimentary components than other middle Eocene granites, which were attributed to partial melting of amphibolite-dominated source under thickened crustal conditions based on high Sr concentration and Sr/Y ratios (Zeng et al., 2011). However, the high Sr and Sr/Y ratios of Haweng granodiorite porphyries may be related to cumulation of plagioclase, and the relative primitive sample shows lower Sr and Sr/Y ratios.

Petrogenesis of Haweng Granodiorite Porphyry
Partial Melting During Prograde Metamorphism in the Himalaya

Many studies suggested that the GHS underwent partial melting as early as the stage of prograde metamorphism (see review in Zhang et al., 2017); however, anatexis records are much less and later than that for the prograde metamorphism. Records of early to middle Eocene prograde metamorphism were reported in several Himalayan domes, such as Mabja (54–52 Ma) and Kangmar (51–49 Ma) domes from central Himalaya (Smit et al., 2014), and Yardoi dome (48–36 Ma) from eastern Himalaya (Ding et al., 2016a,b). Furthermore, Eocene prograde metamorphic records have been widely identified in the GHS along the Himalayan front. In the Pakistan and Garhwal Himalayas, prograde metamorphism was accompanied by growth of monazite (45–36 Ma) and garnet (44–38 Ma) (Foster et al., 2000; Stübner et al., 2014). In the Nepal Himalaya, pervasive prograde metamorphism has initiated as early as early–middle Eocene, such as Karnali Klippe (41–38 Ma, Soucy La Roche et al., 2018), Jajarkot klipe (44–33 Ma, Soucy La Roche et al., 2019), Jumla region (43–33 Ma, Carosi et al., 2010; 41–38 Ma, Gibson et al., 2016; 48–30 Ma, Braden et al., 2017), Annapurna region (38–30, Corrie and Kohn, 2011; 43–36 Ma, Iaccarino et al., 2015; 48–30 Ma, Larson and Cottle, 2015; 48–45, Carosi et al., 2016; 43–30 Ma for the western part, Gibson et al., 2016), and Everest region (*ca.* 45 Ma, Catlos et al., 2002; 40–27 Ma, Cottle et al., 2009). Besides the aforementioned prograde metamorphism, the mineral chemistry of monazite can record the process of anatexis (Gibson et al., 2004; Kohn et al., 2005). Based on the trace elements of analyzed monazites, Braden et al. (2017) speculated the lower GHS in the Jumla region, western Nepal, underwent partial melting as early as *ca.* 40 Ma, as indicated by increase in Y and HREEs of monazite related to
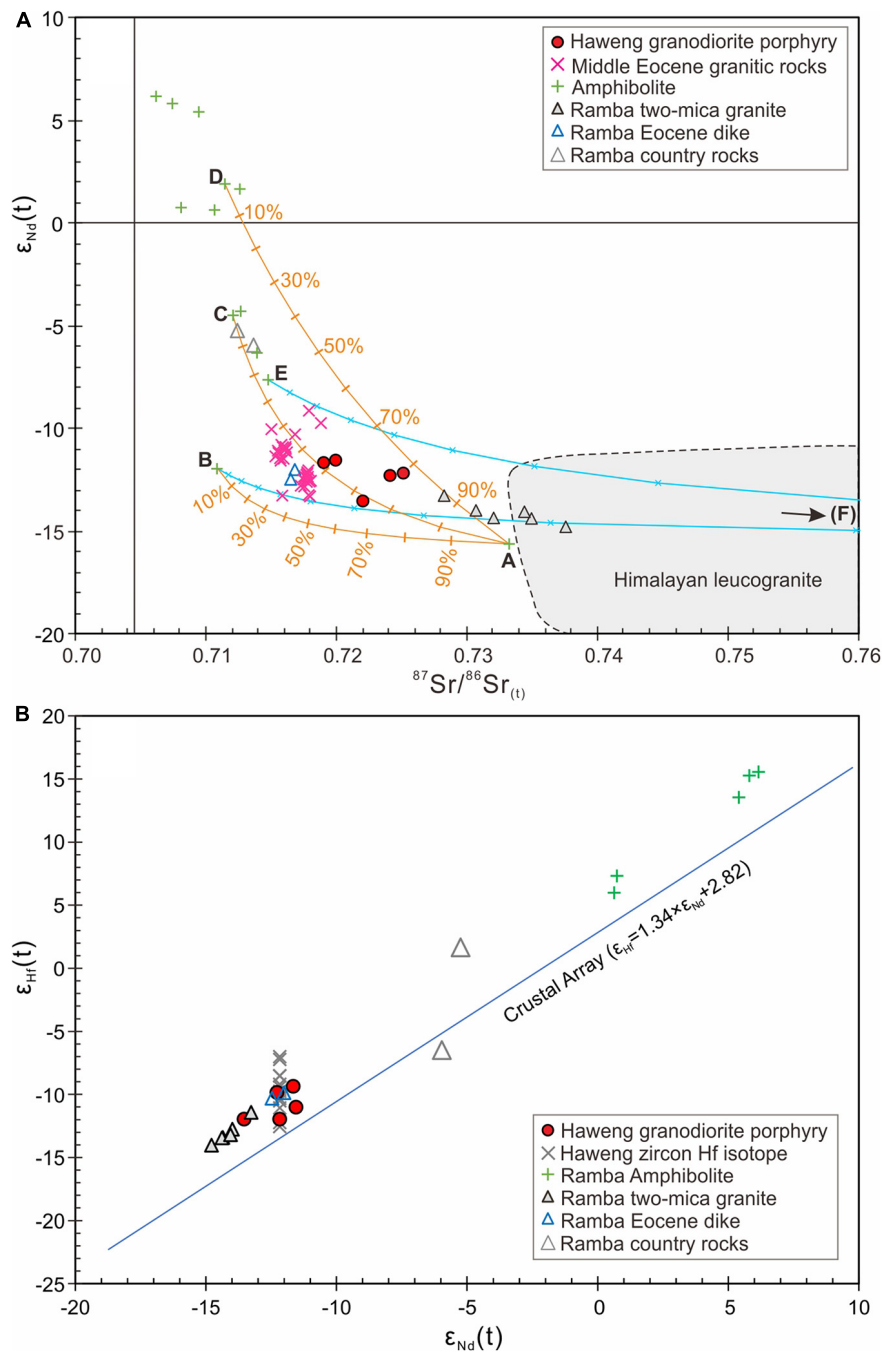
explanation is that the decreases in Sr and Eu due to fractionation of K-feldspar were balanced by other process enriching them, most likely by the cumulation of plagioclases. This is evidenced by the widespread existence of plagioclase phenocrysts. The plagioclase has larger partition coefficients of Ba in more felsic magma (0.5–1.5 for $SiO_2 > 70$ wt.%) than intermediate melts (0.1–0.5 for $60 < SiO_2 < 70$ wt.%) (Laurent et al., 2013). The fractional crystallization of plagioclase would lead to increase in Ba during early magma evolution (Pl-1 in **Figure 5H**), whereas it results in decrease in Ba in more felsic magma (Pl-2 in **Figure 5H**). The middle Eocene granites and Ramba Miocene granites show evolutional trend controlled by fractionation of plagioclase in contrast with the Haweng granodiorite porphyries dominated by K-feldspar (**Figure 5H**). The variation of major and trace elements for Haweng granodiorite porphyries would involve multiple processes of magma evolution, including earlier cumulation of plagioclase and later fractionation of K-feldspar. The more complicated process of Haweng granodiorite porphyry implies there existed a much larger scale of magma than that exposed on the outcrops.

The Haweng granodiorite porphyries were plotted in the scope of amphibolites in the Sr-Nd diagram; thus, they can result from partial melting of mixing component of different amphibolites

FIGURE 7 | (A) Sr–Nd and **(B)** Nd–Hf isotope systematics of Haweng granodiorite porphyries and related rocks. The end-member components for amphiolites (A: T0389-17; B: T0394-6; C: T0321-08; D: T0394-21; E: T0394-8) and metapelite (F: T0321-12) are from Zeng et al. (2009) and Zeng et al. (2011). Data sources: amphibolite: Zeng et al. (2011) and Liu et al. (2014); middle Eocene granitic rocks: Zeng et al. (2011); Aikman et al. (2012), and Hou et al. (2012); Ramba Eocene dikes, country rocks and two-mica granite: Liu et al. (2014); Himalayan leucogranite: Zhang et al. (2004); King et al. (2011), and Guo and Wilson (2012) and references therein.

garnet breakdown during partial melting. However, no direct evidence for anatexis or presence of melt was identified there. Some scholars documented that partial melting occurred during the peak stage of prograde metamorphism. For example, Carosi et al. (2015) reported Eocene partial melting (41–36 Ma; monazite U-Th-Pb age) in the form of nanotonalite inclusions from garnets at the base of the GHS in the Kali Gandaki valley (central Nepal) and attributed it to underthrusting of the GHS. As partial melting would dissolve monazite and greatly affect the preservation of early monazite (Rubatto et al., 2001; Kelsey et al., 2008;

Yakymchuk and Brown, 2014; Wang et al., 2017), the melting would consume monazites and erase their records of earlier metamorphism (Gibson et al., 2004; Kohn et al., 2005; Larson et al., 2011). Therefore, the presence of abundant early–middle Eocene monazites generated by prograde metamorphism of the GHS implies the frontal Himalaya should not have undergone large-scale or widespread partial melting.

It is noteworthy that Wang et al. (2013) discovered middle-late Eocene zircon outgrowth (ca. 40–34 Ma) from sillimanite migmatite in Nyalam (central GHS), which was ascribed to muscovite dehydration melting during prograde metamorphism. Recently, Singh (2019) reported zircon rim dating results (46–20 Ma) for tourmaline-bearing leucogranite in west Garhwal and interpreted the ages representing coeval fluid-fluxed partial melting due to exhumation of migmatite zone. The protracted growth of zircon indicates equilibrium partial melt of its source before the final extraction and emplacement (Singh, 2019). The melt remained trapped within a depth of midcrust when there was episodic liberation of fluids and melts resulting in protracted episodic growth of zircon, garnet, and monazite (Foster et al., 2000). However, because of limit flux of aqueous fluids, the fluid-present melting is difficult for generating large volume of granitic rocks, especially for the segregation of melts from source region in deep crust (Prince et al., 2001). Only under suitable pressure and/or temperature conditions could the melts rise through crust and emplace at high-structural level (Singh, 2019). In the Eastern Himalayan Syntaxis, the Namche Barwa complex underwent long-lived (44–7 Ma) high-temperature granulite facies metamorphism and dehydration melting of muscovite and biotite in buried Indian continent (Zhang et al., 2015). Whether these lines of evidence for migmatization and zircon overgrowth indicate large-scale partial melting and granite formation is yet to be resolved, as the leucosomes in migmatite are distinct from the leucogranites in various aspects, and it is difficult to build their genetic relationship (Yang et al., 2019; Wu et al., 2020).

Genetic Mechanism of Haweng Granodiorite Porphyry and Coeval Magmatism

Based on the review of tectonomagmatic records in the early evolution of southern Tibet, it is indicated that there was a north–south compressional setting, and the early prograde metamorphism was difficult to result in large-scale crustal anatexis. Thus, additional mechanism is necessary for the development of Himalayan magmatism, such as heating, decompression, and addition of water. Generally, continental subduction does not directly trigger decompression, and it is not efficient for water supply; thus, heating is a potential mechanism for the magma generation. According to the distribution of middle Eocene magmatic rocks (**Figure 1**), the heat source should be focused beneath this narrow belt along the YTSZ. Zeng et al. (2011) first used slab breakoff model to account for the origin of middle Eocene (44–42 Ma) granitic rocks in Yardoi dome and adjacent areas, which was attributed to partial melting of amphibolite dominated source under high pressure due to juvenile heat induced by slab breakoff.

Although problems arose in the application of breakoff model in orogenic evolution (cf. Garzanti et al., 2018), this model is by far the most plausible explanation for evolution of southern Tibet. There are various lines of evidence for slab breakoff of Neo-Tethyan slab at around 45 Ma after India–Asia continental collision. Based on tomographic imaging of the mantle under Tibet, Van der Voo et al. (1999) found several high-velocity anomalies, and one of the southern zones was interpreted as remnants of oceanic lithospheric slab. Later, Negredo et al. (2007) estimated the slab breakoff occurred at ca. 44–48 Ma according to paleomagnetic reconstructions and tomographical characters. Kohn and Parkinson (2002) also got breakoff time of ca. 45 Ma on the basis of ages of ultrahigh-pressure (UHP) rocks from the western Himalaya and related records. The UHP eclogite in the Kaghan Valley recorded very rapid exhumation rate from ~100 to ~35 km during ca. 46 to 44 Ma (Parrish et al., 2006), agreeing with breakoff model. Ji et al. (2016) identified OIB (oceanic island basalt)–type gabbro of 45 Ma, derived from partial melting of asthenosphere, which was used to constrain the breakoff time of Neo-Tethyan slab for the middle–east part of the orogenic belt. In combination with coeval geological records, it is proposed that the Neo-Tethyan slab underwent a full-scale detachment (Ji et al., 2016). The breakoff resulted in the cessation of Gangdese arc magmatism (45–40 Ma) to the north of the YTSZ because the subducted continental lithosphere rotated upward to come against the base of the overriding plate (Chemenda et al., 2000) and shielded the active continental margin (the Lhasa terrane) from the convective heat provided previously by corner flow in the mantle wedge during oceanic slab subduction. The breakoff model is also consistent with the clear deceleration of convergence between India and Asia from 8 to 10 to 4 to 6 cm per year at ca. 45 Ma (cf. Patriat and Achache, 1984; van Hinsbergen et al., 2011), possibly due to loss of slab pull after slab breakoff. This study identified new outcrops for middle Eocene magmatism in Langkazi area along the northern Himalayan margin. The variable geochemical compositions of Haweng granodiorite porphyries indicated complicated process of magmatic evolution at depth, implying that the magma scale in the study area should be much larger than that exposed on the outcrops.

CONCLUSION

Based on review of the early to middle Eocene tectonic, metamorphic, and magmatic evolution of the Himalayan orogen, we conducted zircon and titanite U–Pb dating, zircon Hf isotope analyses, whole-rock element, and Sr–Nd–Hf isotope analyses for the newly found Haweng granodiorite porphyries and came to the following conclusions.

(1) The Haweng granodiorite porphyries were generated at ca. 45 Ma, supporting the existence of middle Eocene magmatic belt along the YTSZ. Furthermore, the Langkazi–Ramba area developed a younger thermal event of ca. 30 Ma.

(2) The Haweng granodiorite porphyries display variable element and isotopic compositions, such as Na_2O, K_2O, Rb, Sr, and Ba contents and Rb/Sr and $^{87}Sr/^{86}Sr_{(t)}$ ratios, which indicated magma evolution process involving cumulation of plagioclase and crystal fractionation of K-feldspar. The complicated magma evolution process implies that a much larger scale of magma may occur beneath the less exposed outcrops.

(3) Although early to middle Eocene prograde metamorphism was widespread in the Himalayan orogenic belt, the evidence for accompanied anatexis was sparse. The Haweng granodiorite porphyries and the east–west trending magmatic belt of middle Eocene were attributed to breakoff of the Neo-Tethyan slab at around 45 Ma.

DATA AVAILABILITY STATEMENT

All datasets generated for this study are included in the article/**Supplementary Material**.

AUTHOR CONTRIBUTIONS

W-QJ and F-YW designed the study. W-QJ, F-YW, WC, Z-CL, J-GW, and CZ conducted the fieldwork. W-QJ, X-CL, and ZZ performed the experiments. W-QJ, X-CL, and J-MW wrote the manuscript. All the authors participated in discussion of the study.

FUNDING

ACKNOWLEDGMENTS

SUPPLEMENTARY MATERIAL

The Supplementary Material for this article can be found online at: https://www.frontiersin.org/articles/10.3389/feart.2020.00236/full#supplementary-material

REFERENCES

Aikman, A. B., Harrison, T. M., and Hermann, J. (2012). The origin of Eo-and Neo-himalayan granitoids, Eastern Tibet. *J. Asian Earth Sci.* 58, 143–157. doi: 10.1016/j.jseaes.2012.05.018

Aikman, A. B., Harrison, T. M., and Lin, D. (2008). Evidence for early (> 44 Ma) Himalayan crustal thickening, Tethyan Himalaya, southeastern Tibet. *Earth Planet. Sci. Lett.* 274, 14–23. doi: 10.1016/j.epsl.2008.06.038 doi: 10.1016/j.chemgeo.2004.01.003

Braden, Z., Godin, L., and Cottle, J. M. (2017). Segmentation and rejuvenation of the Greater Himalayan sequence in western Nepal revealed by *in situ* U–Th/Pb monazite petrochronology. *Lithos* 284, 751–765. doi: 10.1016/j.lithos.2017.04.023

Burchfiel, B. C., Zhiliang, C., Hodges, K. V., Yuping, L., Royden, L. H., and Changrong, D. (1992). The south tibetan detachment system, himalayan orogen: extension contemporaneous with and parallel to shortening in a collisional mountain belt. *Geol. Soc. Am. Spec. Pap.* 269, 1–41. doi: 10.1130/spe269-p1

Carosi, R., Montomoli, C., Iaccarino, S., Massonne, H.-J., Rubatto, D., Langone, A., et al. (2016). Middle to late Eocene exhumation of the Greater Himalayan Sequence in the Central Himalayas: progressive accretion from the Indian plate. *Geol. Soc. Am. Bull.* 128, 1571–1592. doi: 10.1130/b31471.1

Carosi, R., Montomoli, C., Iaccarino, S., and Visonà, D. (2019). "Structural evolution, metamorphism and melting in the Greater Himalayan Sequence in central-western Nepal," in *Himalayan Tectonics: A Modern Synthesis*, eds P. J. Treloar, and M. P. Searle (Berkeley, CA: Geological Society of London Special Publication), 305–323. doi: 10.1144/sp483.3

Carosi, R., Montomoli, C., Langone, A., Turina, A., Cesare, B., Iaccarino, S., et al. (2015). "Eocene partial melting recorded in peritectic garnets from kyanite-gneiss, Greater Himalayan Sequence, central Nepal," in *Proceedings of the 29th Himalaya-Karakoram-Tibet Workshop*, Lucca, 111–129. doi: 10.1144/sp412.1

Carosi, R., Montomoli, C., Rubatto, D., and Visonà, D. (2010). Late Oligocene high-temperature shear zones in the core of the Higher Himalayan Crystallines (Lower Dolpo, western Nepal). *Tectonics* 29:TC4029. doi: 10.1029/2008TC002400

Catlos, E. J., Harrison, T. M., Manning, C. E., Grove, M., Rai, S. M., Hubbard, M. S., et al. (2002). Records of the evolution of the Himalayan orogen from *in situ* Th–Pb ion microprobe dating of monazite: eastern Nepal and western Garhwal. *J. Asian Earth Sci.* 20, 459–479. doi: 10.1016/s1367-9120(01)00039-6

Chemenda, A. I., Burg, J.-P., and Mattauer, M. (2000). Evolutionary model of the Himalaya–Tibet system: geopoem: based on new modelling, geological and geophysical data. *Earth Planet. Sci. Lett.* 174, 397–409. doi: 10.1016/s0012-821x(99)00277-0

Chen, L., Qin, K.-Z., Li, G.-M., Li, J.-X., Xiao, B., Zhao, J.-X., et al. (2015). Zircon U–Pb ages, geochemistry, and Sr–Nd–Pb–Hf isotopes of the Nuri intrusive rocks in the Gangdese area, southern Tibet: Constraints on timing, petrogenesis, and tectonic transformation. *Lithos* 212, 379–396. doi: 10.1016/j.lithos.2014.11.014

Cherniak, D. J., and Watson, E. B. (2001). Pb diffusion in zircon. *Chem. Geol.* 172, 5–24. doi: 10.1016/s0009-2541(00)00233-3

Corrie, S. L., and Kohn, M. J. (2011). Metamorphic history of the central Himalaya, Annapurna region, Nepal, and implications for tectonic models. *Geol. Soc. Am. Bull.* 123, 1863–1879. doi: 10.1130/b30376.1

Cottle, J. M., Searle, M. P., Horstwood, M. S., and Waters, D. J. (2009). Timing of midcrustal metamorphism, melting, and deformation in the Mount Everest region of southern Tibet revealed by U (-Th)-Pb geochronology. *J. Geol.* 117, 643–664. doi: 10.1086/605994

Debon, F., Le Fort, P., Sheppard, S. M., and Sonet, J. (1986). The four plutonic belts of the Transhimalaya-Himalaya: A chemical, mineralogical, isotopic, and chronological synthesis along a Tibet-Nepal section. *J. Petrol.* 27, 219–250. doi: 10.1093/petrology/27.1.219

de Sigoyer, J., Chavagnac, V., Blichert-Toft, J., Villa, I. M., Luais, B., Guillot, S., et al. (2000). Dating the Indian continental subduction and collisional thickening in

the northwest Himalaya: multichronology of the Tso Morari eclogites. *Geology* 28, 487–490. doi: 10.1130/0091-7613(2000)028<0487:dticsa>2.3.co;2

Ding, H., Zhang, Z., Dong, X., Tian, Z., Xiang, H., Mu, H., et al. (2016a). Early Eocene (c. 50 Ma) collision of the Indian and Asian continents: constraints from the North Himalayan metamorphic rocks, southeastern Tibet. *Earth Planet. Sci. Lett.* 435, 64–73. doi: 10.1016/j.epsl.2015.12.006

Ding, H., Zhang, Z., Hu, K., Dong, X., Xiang, H., and Mu, H. (2016b). P–T–t–D paths of the North Himalayan metamorphic rocks: implications for the Himalayan orogeny. *Tectonophysics* 683, 393–404. doi: 10.1016/j.tecto.2016.06.035

Ding, L., Kapp, P., and Wan, X. Q. (2005). Paleocene–Eocene record of ophiolite obduction and initial India-Asia collision, south central Tibet. *Tectonics* 24:TC3001. doi: 10.1029/2004tc001729

Elhlou, S., Belousova, E., Griffin, W. L., Pearson, N. J., and O'reilly, S. Y. (2006). Trace element and isotopic composition of GJ red zircon standard by laser ablation. *Geochim. Cosmochim. Acta* 70:A158.

Foster, G., Kinny, P., Vance, D., Prince, C., and Harris, N. (2000). The significance of monazite U–Th–Pb age data in metamorphic assemblages; a combined study of monazite and garnet chronometry. *Earth Planet. Sci. Lett.* 181, 327–340. doi: 10.1016/s0012-821x(00)00212-0

Gao, L., Zeng, L., and Xie, K. (2012). Eocene high grade metamorphism and crustal anatexis in the North Himalayan Gneiss Domes, Southern Tibet. *Chin. Sci. Bull.* 57, 639–650. doi: 10.1007/s11434-011-4805-4

Garzanti, E., Radeff, G., and Malusà, M. G. (2018). Slab breakoff: a critical appraisal of a geological theory as applied in space and time. *Earth Sci. Rev.* 177, 303–319. doi: 10.1016/j.earscirev.2017.11.012

Gibson, H. D., Carr, S. D., Brown, R. L., and Hamilton, M. A. (2004). Correlations between chemical and age domains in monazite, and metamorphic reactions involving major pelitic phases: an integration of ID-TIMS and SHRIMP geochronology with Y–Th–U X-ray mapping. *Chem. Geol.* 211, 237–260. doi: 10.1016/j.chemgeo.2004.06.028

Gibson, R., Godin, L., Kellett, D. A., Cottle, J. M., and Archibald, D. (2016). Diachronous deformation along the base of the Himalayan metamorphic core, west–central Nepal. *Geol. Soc. Am. Bull.* 128, 860–878. doi: 10.1130/b31328.1

Guan, Q., Zhu, D.-C., Zhao, Z.-D., Dong, G.-C., Zhang, L.-L., Li, X.-W., et al. (2012). Crustal thickening prior to 38 Ma in southern Tibet: evidence from lower crust-derived adakitic magmatism in the Gangdese Batholith. *Gondwana Res.* 21, 88–99. doi: 10.1016/j.gr.2011.07.004

Guo, Z., and Wilson, M. (2012). The Himalayan leucogranites: constraints on the nature of their crustal source region and geodynamic setting. *Gondwana Res.* 22, 360–376. doi: 10.1016/j.gr.2011.07.027

Harris, N., and Massey, J. (1994). Decompression and anatexis of Himalayan metapelites. *Tectonics* 13, 1537–1546. doi: 10.1029/94tc01611

Hodges, K. V. (2000). Tectonics of the Himalaya and southern Tibet from two perspectives. *Geol. Soc. Am. Bull.* 112, 324–350. doi: 10.1130/0016-7606(2000)112<324:tothas>2.0.co;2

Hou, Z.-Q., Zheng, Y.-C., Zeng, L.-S., Gao, L.-E., Huang, K.-X., Li, W., et al. (2012). Eocene-Oligocene granitoids in southern Tibet: constraints on crustal anatexis and tectonic evolution of the Himalayan orogen. *Earth Planet. Sci. Lett.* 349, 38–52. doi: 10.1016/j.epsl.2012.06.030

Hu, X., Garzanti, E., Wang, J., Huang, W., An, W., and Webb, A. (2016). The timing of India-Asia collision onset – Facts, theories, controversies. *Earth Sci. Rev.* 160, 264–299. doi: 10.1016/j.earscirev.2016.07.014

Iaccarino, S., Montomoli, C., Carosi, R., Massonne, H.-J., Langone, A., and Visonà, D. (2015). Pressure–temperature–time–deformation path of kyanite-bearing migmatitic paragneiss in the Kali Gandaki valley (Central Nepal): investigation of Late Eocene–Early Oligocene melting processes. *Lithos* 231, 103–121. doi: 10.1016/j.lithos.2015.06.005

Ji, W.-Q., Wu, F.-Y., Chung, S.-L., Li, J.-X., and Liu, C.-Z. (2009). Zircon U–Pb geochronology and Hf isotopic constraints on petrogenesis of the Gangdese batholith, southern Tibet. *Chem. Geol.* 262, 229–245. doi: 10.1016/j.chemgeo.2009.01.020

Ji, W.-Q., Wu, F.-Y., Chung, S.-L., Wang, X.-C., Liu, C.-Z., Li, Q.-L., et al. (2016). Eocene Neo-Tethyan slab breakoff constrained by 45 Ma oceanic island basalt–type magmatism in southern Tibet. *Geology* 44, 283–286. doi: 10.1130/g37612.1

Ji, W.-Q., Wu, F.-Y., Liu, C.-Z., and Chung, S.-L. (2012). Early Eocene crustal thickening in southern Tibet: new age and geochemical constraints from the Gangdese batholith. *J. Asian Earth Sci.* 53, 82–95. doi: 10.1016/j.jseaes.2011.08.020

Ji, W.-Q., Wu, F.-Y., Liu, X.-C., Liu, Z.-C., Zhang, C., Liu, T., et al. (2020). Pervasive Miocene melting of thickened crust from the Lhasa terrane to Himalaya, southern Tibet and its constraint on generation of Himalayan leucogranite. *Geochim. Cosmochim. Acta* 278, 137–156. doi: 10.1016/j.gca.2019.07.048

Kaneko, Y., Katayama, I., Yamamoto, H., Misawa, K., Ishikawa, M., Rehman, H., et al. (2003). Timing of Himalayan ultrahigh-pressure metamorphism: sinking rate and subduction angle of the Indian continental crust beneath Asia. *J. Metamorphic Geol.* 21, 589–599. doi: 10.1046/j.1525-1314.2003.00466.x

Kelsey, D., Clark, C., and Hand, M. (2008). Thermobarometric modelling of zircon and monazite growth in melt-bearing systems: examples using model metapelitic and metapsammitic granulites. *J. Metamorphic Geol.* 26, 199–212. doi: 10.1111/j.1525-1314.2007.00757.x

King, J., Harris, N., Argles, T., Parrish, R., and Zhang, H. (2011). Contribution of crustal anatexis to the tectonic evolution of Indian crust beneath southern Tibet. *Geol. Soc. Am. Bull.* 123, 218–239. doi: 10.1130/b30085.1

Kohn, M., Wieland, M., Parkinson, C., and Upreti, B. (2005). Five generations of monazite in Langtang gneisses: implications for chronology of the Himalayan metamorphic core. *J. Metamorphic Geol.* 23, 399–406. doi: 10.1111/j.1525-1314.2005.00584.x

Kohn, M. J., and Parkinson, C. D. (2002). Petrologic case for Eocene slab breakoff during the Indo-Asian collision. *Geology* 30, 591–594. doi: 10.1130/0091-7613(2002)030<0591:PCFESB>2.0.CO;2

Larson, K. P., and Cottle, J. M. (2015). Initiation of crustal shortening in the Himalaya. *Terra Nova* 27, 169–174. doi: 10.1111/ter.12145

Larson, K. P., Cottle, J. M., and Godin, L. (2011). Petrochronologic record of metamorphism and melting in the upper Greater Himalayan sequence, Manaslu–Himal Chuli Himalaya, west–central Nepal. *Lithosphere* 3, 379–392. doi: 10.1130/l149.1

Laurent, O., Doucelance, R., Martin, H., and Moyen, J.-F. (2013). Differentiation of the late-Archaean sanukitoid series and some implications for crustal growth: insights from geochemical modelling on the Bulai pluton, Central Limpopo Belt, South Africa. *Precambrian Res.* 227, 186–203. doi: 10.1016/j.precamres.2012.07.004

Le Fort, P. (1996). "Evolution of the Himalaya," in *The Tectonic Evolution of Asia*, eds A. Yin and T. M. Harrison (Cambridge: Cambridge University Press), 95–109.

Li, X. H., Liu, Y., Li, Q. L., Guo, C. H., and Chamberlain, K. R. (2009). Precise determination of Phanerozoic zircon Pb/Pb age by multicollector SIMS without external standardization. *Geochem. Geophys. Geosyst.* 10:Q04010. doi: 10.1029/2009GC002400

Liu, Z. C., Wu, F. Y., Ji, W. Q., Wang, J. G., and Liu, C. Z. (2014). Petrogenesis of the Ramba leucogranite in the Tethyan Himalaya and constraints on the channel flow model. *Lithos* 208, 118–136. doi: 10.1016/j.lithos.2014.08.022

Ludwig, K. R. (2003). *User's Manual for Isoplot 3.00, a Geochronological Toolkit for Microsoft Excel*. Berkeley, CA: Geological Society of London, 25–32.

Ma, L., Wang, B.-D., Jiang, Z.-Q., Wang, Q., Li, Z.-X., Wyman, D. A., et al. (2014). Petrogenesis of the early Eocene adakitic rocks in the Napuri area, southern Lhasa: partial melting of thickened lower crust during slab break-off and implications for crustal thickening in southern Tibet. *Lithos* 196, 321–338. doi: 10.1016/j.lithos.2014.02.011

Nábĕlek, J., Hetényi, G., Vergne, J., Sapkota, S., Kafle, B., Jiang, M., et al. (2009). Underplating in the Himalaya-Tibet collision zone revealed by the Hi-CLIMB experiment. *Science* 325, 1371–1374. doi: 10.1126/science.1167719

Negredo, A. M., Replumaz, A., Villaseñor, A., and Guillot, S. (2007). Modeling the evolution of continental subduction processes in the Pamir–Hindu Kush region. *Earth Planet. Sci. Lett.* 259, 212–225. doi: 10.1016/j.epsl.2007.04.043

Parrish, R. R., Gough, S. J., Searle, M. P., and Waters, D. J. (2006). Plate velocity exhumation of ultrahigh-pressure eclogites in the Pakistan Himalaya. *Geology* 34, 989–992.

Paton, C., Woodhead, J. D., Hellstrom, J. C., Hergt, J. M., Greig, A., and Maas, R. (2010). Improved laser ablation U-Pb zircon geochronology through robust downhole fractionation correction. *Geochem. Geophys. Geosyst.* 11:Q0AA06. doi: 10.1029/2009GC002618

Patriat, P., and Achache, J. (1984). India–Eurasia collision chronology has implications for crustal shortening and driving mechanism of plates. *Nature* 311, 615–621. doi: 10.1038/311615a0

Prince, C., Harris, N., and Vance, D. (2001). Fluid-enhanced melting during prograde metamorphism. *Geochem. Geophys. Geosyst.* 158, 233–241. doi: 10.1144/jgs.158.2.233

Pullen, A., Kapp, P., DeCelles, P. G., Gehrels, G. E., and Ding, L. (2011). Cenozoic anatexis and exhumation of Tethyan Sequence rocks in the Xiao Curia Range, Southwest Tibet. *Tectonophysics* 501, 28–40. doi: 10.1016/j.tecto.2011.01.008

Ratschbacher, L., Frisch, W., Liu, G., and Chen, C. (1994). Distributed deformation in southern and western Tibet during and after the India-Asia collision. *J. Geophys. Res.* 99, 19917–19945. doi: 10.1029/94jb00932

Rubatto, D., Williams, I. S., and Buick, I. S. (2001). Zircon and monazite response to prograde metamorphism in the Reynolds Range, central Australia. *Contrib. Mineral. Petrol.* 140, 458–468. doi: 10.1007/pl00007673

Schmitz, M. D., and Bowring, S. A. (2001). U-Pb zircon and titanite systematics of the Fish Canyon Tuff: an assessment of high-precision U-Pb geochronology and its application to young volcanic rocks. *Geochim. Cosmochim. Acta* 65, 2571–2587. doi: 10.1016/s0016-7037(01)00616-0

Scott, D. J., and St-Onge, M. R. (1995). Constrains on Pb closure temperature in titanite based on rocks from the Ungava orogen, Canada: implication for U-Pb geochronology and P-T-t path determination. *Geology* 23, 1123–1126.

Searle, M. (2013). Crustal melting, ductile flow, and deformation in mountain belts: cause and effect relationships. *Lithosphere* 5, 547–554. doi: 10.1130/rf.l006.1

Searle, M., Cottle, J., Streule, M., and Waters, D. (2010). Crustal melt granites and migmatites along the Himalaya: melt source, segregation, transport and granite emplacement mechanisms. *Earth Environ. Sci. Trans. R. Soc. Edinb.* 100, 219–233. doi: 10.1017/s175569100901617x

Searle, M., Windley, B., Coward, M., Cooper, D., Rex, A., Rex, D., et al. (1987). The closing of Tethys and the tectonics of the Himalaya. *Geol. Soc. Am. Bull.* 98, 678–701.

Shellnutt, J. G., Lee, T.-Y., Brookfield, M. E., and Chung, S.-L. (2014). Correlation between magmatism of the Ladakh Batholith and plate convergence rates during the India–Eurasia collision. *Gondwana Res.* 26, 1051–1059. doi: 10.1016/j.gr.2013.09.006

Singh, S. (2019). Protracted zircon growth in migmatites and *in situ* melt of Higher Himalayan Crystallines: U-Pb ages from Bhagirathi Valley, NW Himalaya, India. *Geosci. Front.* 10, 793–809. doi: 10.1016/j.gsf.2017.12.014

Sláma, J., Košler, J., Condon, D. J., Crowley, J. L., Gerdes, A., Hanchar, J. M., et al. (2008). Plešovice zircon—a new natural reference material for U–Pb and Hf isotopic microanalysis. *Chem. Geol.* 249, 1–35. doi: 10.1016/j.chemgeo.2007.11.005

Smit, M. A., Hacker, B. R., and Lee, J. (2014). Tibetan garnet records early Eocene initiation of thickening in the Himalaya. *Geology* 42, 591–594. doi: 10.1130/g35524.1

Soucy La Roche, R., Godin, L., Cottle, J. M., and Kellett, D. A. (2018). Preservation of the early evolution of the Himalayan middle crust in foreland klippen: insights from the Karnali klippe, west Nepal. *Tectonics* 37, 1161–1193. doi: 10.1002/2017tc004847

Soucy La Roche, R., Godin, L., Cottle, J. M., and Kellett, D. A. (2019). Tectonometamorphic evolution of the tip of the Himalayan metamorphic core in the Jajarkot klippe, west Nepal. *J. Metamorphic Geol.* 37, 239–269. doi: 10.1111/jmg.12459

Stübner, K., Grujic, D., Parrish, R. R., Roberts, N. M., Kronz, A., Wooden, J., et al. (2014). Monazite geochronology unravels the timing of crustal thickening in NW Himalaya. *Lithos* 210, 111–128. doi: 10.1016/j.lithos.2014.09.024

Sun, S.-S., and McDonough, W. F. (1989). "Chemical and isotopic systematics of oceanic basalts: implications for mantle composition and processes," in *Magmatism in the Ocean Basins*, Vol. 42, eds A. D. Saunders, and M. J. Norry (Berkeley, CA: Geological Society of London Special Publication), 313–345. doi: 10.1144/gsl.sp.1989.042.01.19

Van der Voo, R., Spakman, W., and Bijwaard, H. (1999). Tethyan subducted slabs under India. *Earth Planet. Sci. Lett.* 171, 7–20. doi: 10.1016/S0012-821X(99)00131-4

van Hinsbergen, D. J., Steinberger, B., Doubrovine, P. V., and Gassmöller, R. (2011). Acceleration and deceleration of India–ŘAsia convergence since the Cretaceous: Roles of mantle plumes and continental collision. *J. Geophys. Res. Solid Earth* 116, B06101. doi: 10.1029/2010JB008051

Vervoort, J. D., Patchett, P. J., Blichert-Toft, J., and Albarède, F. (1999). Relationships between Lu–Hf and Sm–Nd isotopic systems in the global sedimentary system. *Earth Planet. Sci. Lett.* 168, 79–99. doi: 10.1016/s0012-821x(99)00047-3

Wang, C., Ding, L., Zhang, L.-Y., Kapp, P., Pullen, A., and Yue, Y.-H. (2016). Petrogenesis of Middle–Late Triassic volcanic rocks from the Gangdese belt, southern Lhasa terrane: implications for early subduction of Neo-Tethyan oceanic lithosphere. *Lithos* 262, 320–333. doi: 10.1016/j.lithos.2016.07.021

Wang, J., Zhang, J., and Wang, X. (2013). Structural kinematics, metamorphic P–T profiles and zircon geochronology across the Greater H imalayan Crystalline Complex in south-central T ibet: implication for a revised channel flow. *J. Metamorphic Geol.* 31, 607–628. doi: 10.1111/jmg.12036

Wang, J.-M., Wu, F.-Y., Rubatto, D., Liu, S.-R., Zhang, J.-J., Liu, X.-C., et al. (2017). Monazite behaviour during isothermal decompression in pelitic granulites: a case study from Dinggye, Tibetan Himalaya. *Contrib. Mineral. Petrol.* 172:81.

Weis, D., Kieffer, B., Hanano, D., Nobre Silva, I., Barling, J., Pretorius, W., et al. (2007). Hf isotope compositions of US Geological Survey reference materials. *Geochem. Geophys. Geosyst.* 8:Q06006. doi: 10.1029/2006GC001473

Weis, D., Kieffer, B., Maerschalk, C., Barling, J., de Jong, J., Williams, G. A., et al. (2006). High-precision isotopic characterization of USGS reference materials by TIMS and MC-ICP-MS. *Geochem. Geophys. Geosyst.* 7:Q08006. doi: 10.1029/2006GC001283

Wen, D.-R., Liu, D., Chung, S.-L., Chu, M.-F., Ji, J., and Zhang, Q. (2008). Zircon SHRIMP U–Pb ages of the Gangdese Batholith and implications for Neotethyan subduction in southern Tibet. *Chem. Geol.* 252, 191–201. doi: 10.1016/j.chemgeo.2008.03.003

Wiesmayr, G., and Grasemann, B. (2002). Eohimalayan fold and thrust belt: implications for the geodynamic evolution of the NW-Himalaya (India). *Tectonics* 21:1058. doi: 10.1029/2002TC001363

Woodhead, J. D., and Hergt, J. M. (2005). Preliminary appraisal of seven natural zircon reference materials for *in situ* Hf isotope determination. *Geostand. Geoanal. Res.* 29, 183–195. doi: 10.1111/j.1751-908x.2005.tb00891.x

Wu, F. Y., Ji, W. Q., Wang, J. G., Liu, C. Z., Chung, S. L., and Clift, P. D. (2014). Zircon U–Pb and Hf isotopic constraints on the onset time of India-Asia collision. *Am. J. Sci.* 314, 548–579. doi: 10.2475/02.2014.04

Wu, F.-Y., Liu, X.-C., Liu, Z.-C., Wang, R.-C., Xie, L., Wang, J.-M., et al. (2020). Highly fractionated Himalayan leucogranites and associated rare-metal mineralization. *Lithos* 35:105319. doi: 10.1016/j.lithos.2019.105319

Wu, F. Y., Liu, Z. C., Liu, Z. C., and Ji, W. Q. (2015). Himalayan leucogranite: petrogenesis and implications to orogenesis and plateau uplift. *Acta Petrol. Sin.* 31, 1–36.

Wu, F.-Y., Yang, Y.-H., Xie, L.-W., Yang, J.-H., and Xu, P. (2006). Hf isotopic compositions of the standard zircons and baddeleyites used in U–Pb geochronology. *Chem. Geol.* 234, 105–126. doi: 10.1016/j.chemgeo.2006.05.003

Xie, L., Zhang, Y., Zhang, H., Sun, J., and Wu, F. (2008). *In situ* simultaneous determination of trace elements, U–Pb and Lu–Hf isotopes in zircon and baddeleyite. *Chin. Sci. Bull.* 53, 1565–1573. doi: 10.1007/s11434-008-0086-y

Yakymchuk, C., and Brown, M. (2014). Consequences of open-system melting in tectonics. *Geochem. Geophys. Geosyst.* 171, 21–40. doi: 10.1144/jgs2013-039

Yang, L., Liu, X.-C., Wang, J.-M., and Wu, F.-Y. (2019). Is Himalayan leucogranite a product by *in situ* partial melting of the Greater Himalayan Crystalline? A comparative study of leucosome and leucogranite from Nyalam, southern Tibet. *Lithos* 342, 542–556. doi: 10.1016/j.lithos.2019.06.007

Yang, Y.-H., Chu, Z.-Y., Wu, F.-Y., Xie, L.-W., and Yang, J.-H. (2011a). Precise and accurate determination of Sm, Nd concentrations and Nd isotopic compositions in geological samples by MC-ICP-MS. *J. Anal. Atomic Spectrom.* 26, 1237–1244.

Yang, Y.-H., Wu, F.-Y., Xie, L.-W., Yang, J.-H., and Zhang, Y.-B. (2011b). High-precision direct determination of the 87Sr/86Sr isotope ratio of bottled Sr-rich natural mineral drinking water using multiple collector inductively coupled plasma mass spectrometry. *Spectrochim. Acta Part B Atomic Spectrosc.* 66, 656–660. doi: 10.1016/j.sab.2011.07.004

Yang, Y.-H., Zhang, H.-F., Chu, Z.-Y., Xie, L.-W., and Wu, F.-Y. (2010). Combined chemical separation of Lu, Hf, Rb, Sr, Sm and Nd from a single rock digest and precise and accurate isotope determinations of Lu–Hf, Rb–Sr and Sm–Nd isotope systems using Multi-Collector ICP-MS and TIMS. *Int. J. Mass Spectrom.* 290, 120–126. doi: 10.1016/j.ijms.2009.12.011

Yin, A. (2006). Cenozoic tectonic evolution of the Himalayan orogen as constrained by along-strike variation of structural geometry, exhumation history, and foreland sedimentation. *Earth Sci. Rev.* 76, 1–131. doi: 10.1016/j.earscirev.2005.05.004

Zeng, L., and Gao, L. (2017). Cenozoic crustal anatexis and the leucogranites in the Himalayan collisional orogenic belt. *Acta Petrol. Sin.* 33, 1420–1444.

Zeng, L., Gao, L.-E., Tang, S., Hou, K., Guo, C., and Hu, G. (2015). "Eocene magmatism in the Tethyan Himalaya, southern Tibet," in *Tectonics of the Himalaya*, eds S. Mukherjee, R. Carosi, P. A. Van der Beek, B. K. Mukherjee, and D. M. Robinson (Berkeley, CA: Geological Society of London Special Publication), 287–316. doi: 10.1144/sp412.8

Zeng, L., Liu, J., Gao, L., Xie, K., and Wen, L. (2009). Early Oligocene anatexis in the Yardoi gneiss dome, southern Tibet and geological implications. *Chinese Sci. Bull.* 54, 104–112. doi: 10.1007/s11434-008-0362-x

Zeng, L. S., Gao, L. E., Xie, K. J., and Jing, L. Z. (2011). Mid-Eocene high Sr/Y granites in the Northern Himalayan Gneiss Domes: melting thickened lower continental crust. *Earth Planet. Sci. Lett.* 303, 251–266. doi: 10.1016/j.epsl.2011.01.005

Zhang, H., Harris, N., Parrish, R., Kelley, S., Zhang, L., Rogers, N., et al. (2004). Causes and consequences of protracted melting of the mid-crust exposed in the North Himalayan antiform. *Earth Planet. Sci. Lett.* 228, 195–212. doi: 10.1016/j.epsl.2004.09.031

Zhang, Z., Dong, X., Ding, H., Tian, Z., and Xiang, H. (2017). Metamorphism and partial melting of the Himalayan orogen. *Acta Petrol. Sin.* 33, 2313–2341.

Zhang, Z., Xiang, H., Dong, X., Ding, H., and He, Z. (2015). Long-lived high-temperature granulite-facies metamorphism in the Eastern Himalayan orogen, south Tibet. *Lithos* 212-215, 1–15. doi: 10.1016/j.lithos.2014.10.009

Zhao, W., Mechie, J., Brown, L., Guo, J., Haines, S., Hearn, T., et al. (2001). Crustal structure of central Tibet as derived from project INDEPTH wide-angle seismic data. *Geophys. J. Int.* 145, 486–498. doi: 10.1046/j.0956-540x.2001.01402.x